The Pennsylvania State University

The Graduate School

A METHOD TO DESIGN AND DEVELOP ADDITIVELY MANUFACTURED AIRCRAFT ACOUSTIC LINERS

A Thesis in

Additive Manufacturing and Design

by

Andrew T. Swanson

Submitted in Partial Fulfillment
of the Requirements
for the Degree of

Master of Science

August 2023

The thesis of Andrew T. Swanson was reviewed and approved by the following:

Timothy W. Simpson
Paul Morrow Professor of Engineering Design & Manufacturing
Thesis Advisor

Allison M. Beese
Director of the Additive Manufacturing and Design Program
Associate Professor of Material Science and Engineering

Eric Greenwood
Assistant Professor of Aerospace Engineering

Abstract

The freeform geometry enabled by additive manufacturing (AM) gives designers many unique capabilities, which has led to novel uses in numerous engineering applications. One emerging use of these freeform AM structures is in aircraft acoustic liners. Modern aircraft have increasingly adopted acoustic liners to reduce the sound emitted by their turbofan engines to meet acoustic emission requirements. Most current acoustic liners take the form of micro-perforated panel (MPP) absorbers. Although traditional MPPs absorb specific tones well, they do not perform as well over a wide range of frequencies. As future aircraft engines start to utilize high-bypass ratios, acoustic liners that can attenuate a wide range of sound frequencies (low-frequencies in particular) with a reduced form factor are needed. Developing a conventional acoustic liner with adequate broadband absorption that also meets size and weight requirements is challenging, expensive, and time-consuming. Therefore, a new integrated design and development method for aircraft acoustic liners is needed to address this barrier. A rapid design and development workflow that uses AM for creating complex novel acoustic liner geometries is presented. This new methodology can help support the development of acoustic liners that are needed for future aircraft engines by allowing the design space to be expanded and explored in ways previously impossible or too expensive to fabricate.

Table of Contents

List of Figures

List of Tables

List of Symbols

Symbol	Description
α	Absorption coefficient
f	Frequency
f_r	Resonant frequency
f_u	Upper-frequency limit of normal impedance tube
f_l	Lower-frequency limit of normal impedance tube
k	wavenumber
μ	Attenuation
H_{12}	Complex transfer function between two microphones
H_h	Complex transfer function of incident wave from the test sample
H_r	Complex transfer function of reflected wave from the test sample
R	Reflection
p_a	Acoustic pressure
$\overline{p_a}$	Complex conjugate of acoustic pressure
SPL	Sound pressure level
TL	Transmission loss
W_i	Incident plane wave acoustic power on a surface
W_t	Transmitted plane wave acoustic power on a surface
c	Speed of sound
Z	Acoustic impedance
$Z_{\rho c}$	Specific acoustic impedance
Z_{gf}	Acoustic impedance when exposed to a grazing flow
ε	Scalar correction factor
s	Distance between two microphones
w	Width of impedance tube waveguide with a square cross-section
L	Length of Helmholtz resonator neck
A_c	Cross-sectional area
V	Volume of Helmholtz resonator cavity
r	Facesheet hole radius
x_1	Distance from facesheet to microphone one
x_2	Distance from facesheet to microphone two
ρ	Density
K	Compression modulus or bulk modulus
$\tilde{\rho}_{eq}$	Complex mass density
$\widetilde{K}_{eq}$	Complex compression modulus or complex bulk modulus
ω	Angular frequency or pulsation
h	Facesheet thickness
ν	Kinematic viscosity
θ	Real component of acoustic impedance (resistance)
χ	Imaginary component of acoustic impedance (reactance)
ϕ	Percent open area of facesheet in decimal form
η	Dynamic viscosity

σ	Fluid stress tensor
γ	Ratio of specific heat
P_{atm}	Atmospheric pressure
P	Fluid pressure
$\vec{v}$	Fluid velocity vector
Pr	Prandtl's number
v_a	Acoustic particle velocity
t	Time
j	$\sqrt{-1}$
J_n	Ordinary Bessel function of the n^{th} order
N_{mics}	Number of virtual microphone probes
p_{ref}	Reference acoustic pressure
D	Cavity depth
d_{dev}	Facesheet hole diameter deviation
d_{major}	Major diameter of an ellipse
d_{minor}	Minor diameter of an ellipse
d	Nominal facesheet hole diameter
δ	Boundary layer height
M	Mach number
β	General curve fit parameter
x_l	Array of position values sampled along an arbitrary line
C	Surface iso-value
F	Implicit function of TPMS surface
G	Function controlling the transition between two TPMS surfaces
x, y, z	General cartesian coordinates
r_c, ϑ_c, z_c	General cylindrical coordinates
$r_s, \vartheta_s, \varphi_s$	General spherical coordinates

Acknowledgments

First, I would like to give a special thanks to my family for the love, encouragement, patience, opportunities, and support they have given me throughout my years in school. I am very thankful to have you all in my life.

I would also like to thank my advisor Dr. Tim Simpson and the other ASCENT 79 collaborators from Penn State and Raytheon Technologies Research Center for affording me the opportunity to help support this project. I have really enjoyed working on this project, getting to know everyone, and learning so much over the past two years.

I would also like to thank Dr. Allison Beese, Jaclyn Stimely, and the other AMD faculty for all their work in making the AMD graduate program possible. It is truly a unique and remarkable program, and I am fortunate to have been able to experience it.

This work was funded by the Aviation Sustainability Center (ASCENT) project 79 research grant [1]. "ASCENT – the Aviation Sustainability Center – is a cooperative aviation research organization co-led by Washington State University and the Massachusetts Institute of Technology. Also known as the Center of Excellence for Alternative Jet Fuels and Environment, ASCENT is funded by the FAA, NASA, the Department of Defense, Transport Canada, and the Environmental Protection Agency. ASCENT works to create science-based solutions for the aviation industry's biggest challenges. A coalition of 16 leading US research universities and over 60 private sector stakeholders committed to reducing the environmental impact of aviation, ASCENT also works in partnership with international research programs, federal agencies and national laboratories to create an all-inclusive research capability for whatever environmental impact obstacle the aviation industry faces." [2]. Manufacturing and testing facilities were provided by the Pennsylvania State University, the Pennsylvania State University Applied

Research Laboratory, Raytheon Technologies Research Center, and NASA Langley Research Center. The views and opinions expressed in this thesis do not necessarily represent those of other project contributors or the ASCENT organization and its stakeholders.

Chapter 1

Introduction

1.1 Background

According to Crocker and Arenas, "The number of aircraft used for civilian and military air transportation has increased steadily during the last decades. Thus, aircraft noise has been a problem for people living in the vicinity of airports for many years." [3, p. 661]. In addition to affecting the surrounding communities, excess noise can also inhibit an airplane's performance and efficiency [4]. The turbofan engines that power many of the conventional tube and wing aircraft are responsible for much of the noise generated [5]. To reduce the noise these engines create, acoustic liners are often employed to absorb some of the sound energy before it radiates outside of the duct [6]. These liners are often placed inside an engine's nacelle around the inlet and bypass ducts, outside the combustor, and around the turbine exhaust duct [7]. A diagram showing the location of acoustic liners in a typical turbofan engine can be seen in Figure 1.

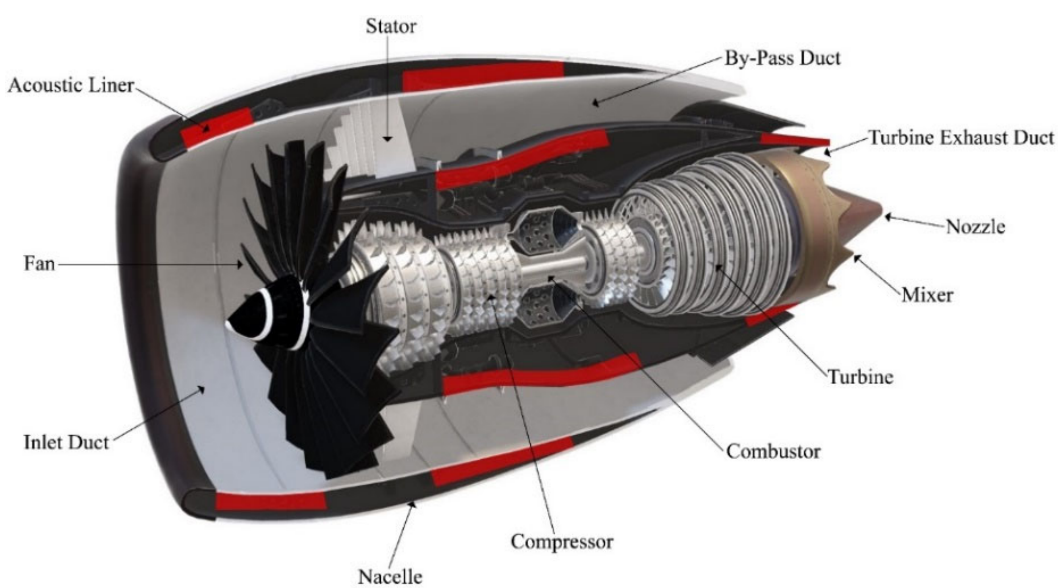

Figure 1. Location of acoustic liners in a typical turbofan engine. Diagram adapted from [7].

The current generation of acoustic liners is known to work well with existing turbofan engine designs; however, they are expected to become less effective in the future as engine designs evolve to meet increasingly stringent efficiency, emission, and performance requirements [5], [8], [9]. To meet these requirements, manufacturers are favoring designs that leverage high bypass ratios (ratio of the mass flow rate of air that bypasses around the core to the mass flow rate of air passing through it) [5], [8], [9]. While these adjustments help satisfy design goals and requirements, they also change the engine's acoustic profile. For example, the acoustic emissions of engine platforms with lower bypass ratios usually consist primarily of jet noise with some additional fan, compressor, combustor, and turbine noise [5], [8], [9]. Although, when high bypass ratios are used, the jet noise component is significantly reduced, and broadband fan noise (low frequencies in particular) becomes dominant [5], [8], [9]. In addition to the fan noise becoming dominant, other sound sources that were a secondary concern in the past (e.g., compressor, combustor, turbine) have become more important factors to consider [5], [8], [9]. The current generation of acoustic liners could potentially be adapted to meet this new profile by increasing their size in both the axial and radial extent, but this is not an ideal approach due to the competing weight and size requirements they would encounter [5], [8], [9]. Hence, existing acoustic liners are expected to become less effective going forward.

1.2 Problem Statement

To address the issue of current acoustic liners being less effective for future engine designs, a new generation of novel liners needs to be designed and developed. For the new generation of liners to succeed, they must provide good broadband sound attenuation (with a focus on low frequencies) while having a small form factor and being manufacturable. Using existing design configurations and development methods to meet these goals would be challenging, expensive, and time-consuming. Therefore, one potential new approach for creating the next generation of acoustic liners is to expand the current design and development workflow to include new design thinking, software tools, and advanced manufacturing techniques. Of particular interest is to integrate additive manufacturing (AM) into the development process [8], [9]. ASTM standard 52900 defines AM as "a process of joining materials to make objects from 3D model data, usually layer upon layer, as opposed to subtractive manufacturing methodologies." [10]. The layered nature of AM gives it many advantages relative to conventional manufacturing techniques. Some of these advantages include the ability to create complex freeform geometry, consolidate assemblies, and customize a component's material composition and weight [11]–[19]. By combining the unique capabilities of AM with other advanced engineering tools in an integrated workflow, the design space for acoustic liners can be expanded and explored in ways previously impossible or too expensive to fabricate.

1.3 Research Objectives and Outline

The main focus of this thesis is to describe and demonstrate an efficient and effective method that supports the design and development of novel AM acoustic liners for future turbofan engines. To achieve this objective, an initial literature review in Chapter 2 explores conventional liners, early research in AM liners/acoustic absorbers, and development methods for aircraft acoustic liners. In Chapter 3, by leveraging the learnings, information, and gaps identified during the literature review, a new AM-focused design and development method is proposed. Following the introduction of the new method, each step of the method is explained in detail in the remainder of Chapter 3. After the new method has been thoroughly described, a single iteration implementing the process is shown in Chapter 4 to test and demonstrate the new design and development method. Finally, Chapter 5 summarizes the research, discusses strengths and weaknesses, and provides potential avenues for future work.

Chapter 2

Literature Review

This chapter presents an initial literature review investigating topics relevant to proposing a new AM-focused acoustic liner design and development methodology. The relevant review topics include key background information on acoustic liner theory, current conventional acoustic liner research, early research in AM liners/acoustic absorbers, and existing acoustic liner design and development methods. The information, learnings, and insights from this chapter serve as a basis for proceeding chapters.

2.1 Review of Conventional Acoustic Liners

For most noise control applications, acoustic absorbers can be grouped into one of three categories [3]. The first of which, in no particular order, are bulk absorbers. *Bulk absorbers* are solid materials with many cavities, channels, and interstices that are open to an external fluid [20]. Typically they reduce noise by turning sound energy into heat as sound waves propagate through them [20]. Common examples include foam, fibreboard, and cloth-like materials [21]. The second group of absorbers are called panel or membrane absorbers. *Membrane absorbers* are structural pieces or barriers that vibrate when exposed to specific sound frequencies, turning the sound energy into mechanical energy [3]. These membrane absorbers are commonly mounted on the walls and ceilings of theaters, auditoriums, and gyms.

The third and final category of absorbers are known as *Helmholtz resonators*, which are acoustic devices consisting of a rigid cavity connected to a small neck section with an open port [3]. When sound acts on the device, the air molecules inside and around the neck section oscillate like a vibrating mass (causing frictional and viscous losses) because the air in the cavity below acts like a spring [3]. Due to a small amount of damping in the system, the resonant peak usually occurs at distinct frequency values [3]. A diagram of a Helmholtz resonator and an equivalent damped spring-mass system often used to describe them can be seen in Figure 2. Also, the equation for the resonant frequency of an undamped Helmholtz resonator with a flanged neck section can be seen in Equation 1 (assuming no boundary effects) [3].

At and around the resonant frequency, the sound absorption of a Helmholtz resonator is at its maximum value, making equation one useful for design. The descriptions of all the variables and symbols used throughout this thesis are listed in the symbols section. Depending on the application, one or more of these acoustic absorber types can be combined to make hybrid absorbers or used as individual units working alone or in tandem with each other.

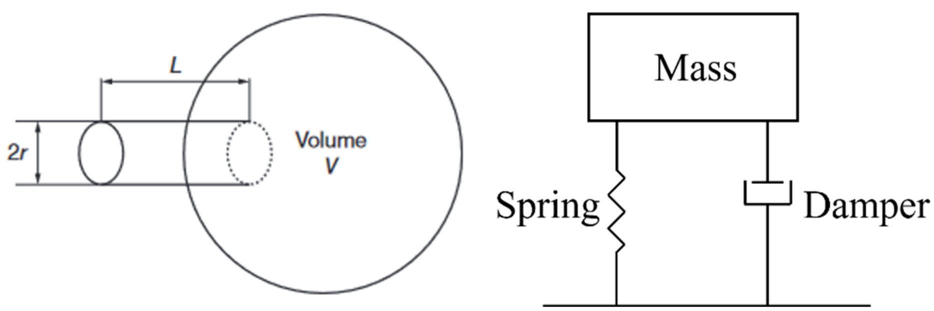

Figure 2. Diagram of a Helmholtz resonator (taken from [3]) and an equivalent damped spring-mass system. The mass component represents the air inside the neck. The spring and damper components model the rigid volume underneath.

$$f_r = \frac{c}{2\pi}\sqrt{\frac{A_c}{(L+1.7r)V}} \tag{1}$$

Due to the harsh environmental conditions and structural requirements of acoustic absorbers in many different applications (like aircraft engine acoustic liners), bulk and membrane absorbers are not always the best option [22]. Therefore, Helmholtz resonator-type absorbers have to be used in these scenarios. However, when reasonably sized, a single Helmholtz resonator's low-frequency tonal absorption behavior is often not ideal and can present a significant design challenge. Consequently, perforated panel absorbers were developed in response to this shortcoming beginning in the 1940s [23]–[29].

Perforated panel absorbers consist of a top facesheet with several holes or slots separated by an enclosed volume (usually filled with air when used in harsh conditions) from a solid backplate [3]. A practical way to think of perforated panel absorbers is as combined arrays of Helmholtz resonators where each facesheet hole makes up an individual unit's neck and pore region. The empty cavity below is shared between all of the different facesheet holes. Combining the resonators in this fashion allows for slightly more broadband absorption at higher frequency values than an individual unit because it increases the cavity spring constant to acoustic mass ratio and distributes resistance throughout the facesheet [3]. This configuration also allows various hole sizes to be used throughout the facesheet, which can additionally help increase wideband absorption [3].

A diagram of an empty cavity extended-reacting perforated panel absorber is shown in Figure 3. The resonance frequency of a perforated panel absorber with sufficiently large diameter circular holes (diameter approximately greater than or equal to three millimeters) and an empty air cavity can be determined using Equation 2 [3]. From Equation 2, it can be seen that the resonance frequency is directly proportional to the facesheet percent open area (POA) and inversely proportional to the facesheet thickness and cavity depth.

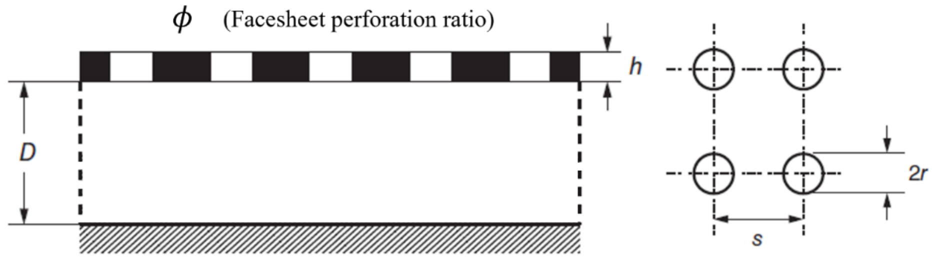

Figure 3. Diagram showing the layout of a typical extended-reacting perforated panel absorber (taken from [3]).

$$f_r = \frac{c}{2\pi}\sqrt{\frac{\phi}{D\left[h + 1.6r\left(1 - 1.47\sqrt{\phi} + 0.47\sqrt[3]{\phi}\,\right) + \sqrt{\frac{8\nu}{\omega}\left(1 + \frac{h}{2r}\right)}\,\right]}} \tag{2}$$

Despite the improvements perforated panel absorbers made over single Helmholtz resonators, they still often lack the broadband sound attenuation required for some applications. One approach that can be utilized to improve broadband sound absorption of perforated panel absorbers is to stack one or more units on top of each other with additional facesheets between them [5], [8], [9], [22], [30], [31]. Stacking perforated panel absorbers on top of each other is often referred to as adding more degrees of freedom (DOF). For example, a single perforated panel absorber would be categorized as a single-degree-of-freedom (SDOF), and two perforated panel absorbers stacked on each other would be categorized as dual-degree-of-freedom (DDOF). Additional DOFs are beneficial because they allow designers to tune the acoustic behavior at additional distinct frequencies, improving broadband attenuation [5]. However, adding more DOFs cause size, cost, and weight to increase while decreasing overall durability, manufacturability, and peak attenuation.

Throughout the late 1950s to the early 1980s, adjustments were made to the facesheets of panel absorbers to improve their effective absorption range. These improvements were achieved by decreasing the facesheet hole diameter to between one and one-half millimeters [22]. Panel absorbers with these smaller facesheet holes are usually called *microperforated panel absorbers*

(MPPs). While this change in hole diameter is relatively simple, it allows for enhanced broadband absorption because the hole size is comparable to the fluid boundary layer, significantly increasing viscous losses as the air rushes in and out of the holes [3]. MPPs extended the wideband attenuation range to approximately one octave relative to the peak frequency for SDOF and a two-octave frequency range for DDOF absorbers [8].

The increased wideband absorption of MPPs makes designing them using single resonant frequency values and knowing that attenuation is maximized at and around that frequency value (e.g., Equations 1 and 2) an oversimplified approach. Instead, other quantities of interest (QOIs), like the acoustic impedance and absorption coefficient, are preferred metrics because they can characterize performance as a function of frequency. The *acoustic impedance* is the ratio of the sound pressure to the acoustic particle velocity at a given point inside some region [3]. The real and imaginary components of acoustic impedance are called resistance and reactance, respectively. *Acoustic resistance* is a measure of the forces dissipating acoustic energy, while *acoustic reactance* describes the efficiency of these energy transfer processes [8].

Another way to think about the acoustic impedance is the amount of opposition a domain provides to a sound wave propagating through it. Equation 3 can be used to approximate the acoustic impedance of an MPP with an empty cavity [9], [22]. However, complex numbers can be challenging to interpret; so, using the acoustic resistance and reactance values to calculate the absorption coefficient is common. The absorption coefficient is the proportion of the sound intensity absorbed by the material or acoustic power absorbed per unit area [3]. Equation 4 can be used to calculate the absorption coefficient from resistance and reactance values [9], [22]. Other methods exist to calculate the acoustic impedance and absorption coefficient, but Equations 3 and 4 provide one of the most straightforward approaches for basic designs. It is important to note that Equation 3 does not consider the non-linear effects that arise when MPPs are exposed to high sound pressure levels (SPL), grazing flows, and bias flows [9].

$$Z = \frac{8\eta h}{\phi\rho c d^2}\left(\sqrt{\frac{\omega\rho d^2}{32\eta}+1}+\frac{\sqrt{2}d^2\sqrt{\frac{\omega\rho}{\eta}}}{2h}\right)+j\left\{\frac{\omega h}{\phi c}\left(\frac{1}{\sqrt{\frac{\omega\rho d^2}{2\eta}+9}}+\frac{16d}{3\pi h}+1\right)-\cot\left(\frac{\omega D}{c}\right)\right\} \quad (3)$$

$$\alpha = \frac{4\theta}{(1+\theta)^2+\chi^2}\,, \quad Re(Z)=\theta\ \&\ Im(Z)=\chi \quad (4)$$

Most of the acoustic liners currently used on modern aircraft engines are either SDOF or DDOF passive honeycomb core MPPs [8]. These MPPs are made by placing one or more honeycomb cores between a solid backplate and perforated facesheet with an adhesive binder at the interfaces to hold them together. Typically, all honeycomb core MPP components are made from an aluminum alloy sheet metal because it is readily available, inexpensive, lightweight, easy to process, and corrosion-resistant. It is important to mention that when thermal loading is high, nickel-based alloys or ceramics with better-suited thermal properties are used instead. While the current manufacturing process is straightforward, it leads to some issues in the final product. Most notably, the binder that is holding everything together can sometimes be a problem, as debonding from cyclic loading during flight and age-related material degradation occurs [8]. Also, the facesheet holes and honeycomb core do not always align well, decreasing overall performance and introducing variability within and between panels. Examples of both SDOF and DDOF honeycomb core MPPs can be seen in Figure 4. Despite these issues, this design configuration continues to see service in many aircraft because they are lightweight, cost-effective, provide reasonable absorption, and the smooth facesheet does not produce excess drag inside the engine when exposed to grazing flow. Most noise attenuation in a honeycomb core and empty cavity MPP occurs at and around the facesheet holes.

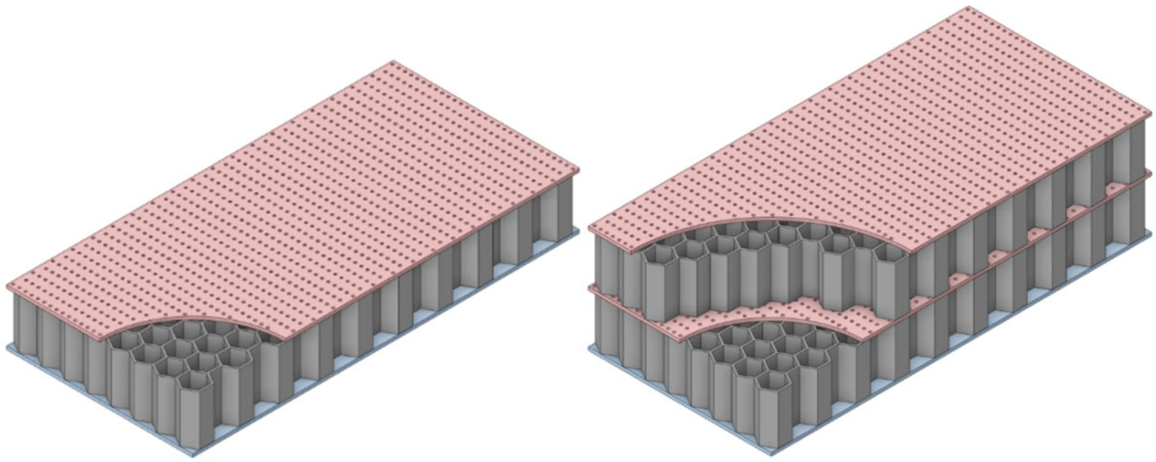

Figure 4. Examples of SDOF and DDOF honeycomb core MPPs that are typically found in aircraft engines (adapted from [5], [7]–[9]).

The main difference between these honeycomb core MPPs and the original hollow cavity design configuration is the honeycomb core section inside the air cavity. The honeycomb core serves two primary purposes. The first of which is adding structural integrity under static loads, like a technician standing on them during maintenance, and during high strain rate impact loads, such as debris strikes during flight (which are rare) [8]. Also, they make the liner locally reacting, meaning sound waves cannot propagate through the liner parallel to the facesheet when exposed to a grazing flow or oblique-incident sound waves concentrating resistance at specific facesheet locations. On the other hand, empty cavity configurations are known as extended-reacting because the resistance is distributed throughout the facesheet. While the sectioning of the cavity has some effect on the absorption behavior, the primary driving factors are the liner's overall size, depth, and facesheet dimensions. As previously mentioned, the size and depth cannot be increased to meet the noise attenuation requirements of future turbofan engines because they would unlikely meet weight and size restrictions in this design configuration.

Methods to address the known issues with conventional honeycomb core liners and improve their overall performance have been an active area of research for the past few decades

[8]. Several different concepts have been proposed, but many of them are unlikely to see wide-scale industrial applications due to cost, manufacturability, and practicality concerns [8]. Nevertheless, several proposed adjustments to existing liners and entirely new design configurations have gained interest and traction in the aircraft acoustic liner community [32]. A few of these concepts can be seen in Figure 5 and are discussed as follows.

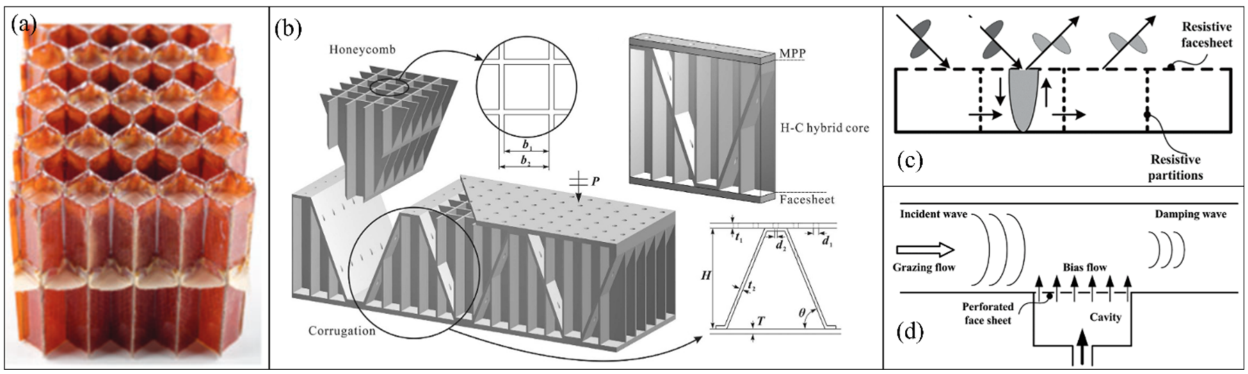

Figure 5. Honeycomb liner core with mesh caps (a) (taken from [5]), acoustic liner with wedge-shaped panels that creates variable cavity depths (b) (taken from [33]), acoustic liner with resistive partitions (c) (taken from [34]), and a diagram of an acoustic liner that has a bias flow applied to the facesheet (d) (taken from [32]).

One common approach (patented in the early 2000s) seen in Figure 5(a) is to take existing SDOF honeycomb core liners and glue one or more mesh caps inside each hexagon at various heights. Essentially the mesh cap allows the SDOF liner to behave like a variable depth multi-DOF liner without the compromises in cost, size, and weight that often accompany the stacking approach. High-fidelity testing performed by Sutliff et al. [5] demonstrated the efficacy of the mesh cap liners over existing SDOF and DDOF liners. A similar concept investigated by Tang et al. [33] added wedge-shaped panels to an MPP's core, as seen in Figure 5(b), giving it a variable-sized air cavity that improved the effective absorption range.

Another way to adjust existing liners suggested by Parrott and Jones [34] was to add perforations to cavity partitions to increase the acoustic resistance, as seen in Figure 5(c). The benefit of these extra perforations is that they increase the total viscous losses (particularly under a grazing flow or oblique incidence) while also decreasing weight. Additionally, compliant core sections that behave like membrane absorbers have been explored by Dannemann et al. [35] as an alternative to the current rigid materials.

These different adjustments and designs are all passive, but other concepts utilizing active systems with in-situ tunability have also been investigated. Tunability in aircraft liners is often achieved using variable geometry sizing and bias flows [32]. For example, Esteve and Johnson [36], Liu [37], and Williams et al. [38] achieved adaptable noise and vibration control devices by using electromechanical mechanisms, piezoelectric materials, and shape memory alloys to vary key dimensions (facesheet hole diameter, cavity depth/shape, etc.). Adaptability can also be achieved by using bias flows through the bottom of a facesheet, as seen in Figure 5(d). Bias flows allow for tunability by controlling the opposing flow velocity, which in turn affects acoustic resistance and reactance values [32]. Also, bias flows can be leveraged to cool acoustic liners in high-temperature environments [9], [32]. Results similar to the bias flow approach can also be achieved with loudspeakers mounted on the backplates of liners through active phase cancelation, as discussed by XuQiang and ZhengTao [32]. These active liners can usually outperform passive liner designs but come with significantly more complexity, cost, and reliability concerns.

2.2 Review of AM Acoustic Liners

As previously mentioned, one of the most significant advantages of AM is its ability to create complex freeform geometries that are impossible or impractical to make with conventional manufacturing processes. Therefore, most interest and initial research into AM acoustic liners and absorbers have revolved around leveraging this geometric design freedom to make novel sound-absorbing structures and metamaterials. A metamaterial is an artificially structured object that obtains its unique properties from its engineered shape rather than its chemical makeup [9], [39]. Most of the proposed AM acoustic liner/absorber concepts can be grouped into one of three categories discussed in the following sections.

2.2.1 Lattices and Cellular Structures

One of the most popular metamaterials that have emerged with the advent of AM are lattices and cellular structures. Lattices and cellular structures are a meso-level design feature consisting of several fundamental unit cells periodically patterned out in three-dimensional space [40]. Due to their numerous input variables and highly tunable properties, they have been extensively used for applications in various fields, such as structural mechanics, heat transfer, electromagnetics, and medicine [41]. The unit cells that make up these lattices can be categorized into three groups: (1) strut-based unit cells, (2) surface-based unit cells, and (3) planar-based unit cells [40]. The unit cells of *strut-based lattices* are made up of thick connected beam elements arranged in either an ordered or stochastic way. Strut-based unit cells are usually based on mathematical shapes, the molecular structure of known materials and elements, or pseudorandom point sampling. The unit cells of *surface-based lattices* are often thick sheets defined by mathematical equations in either cartesian, cylindrical, or spherical space. The negative space around the thick sheets can also be used to define the unit cells, which are coined as skeletal unit cells. The most commonly used equations for surface-based unit cells are triply periodic minimal surfaces (TPMS) such as the gyroid, Schwarz D, and lidinoid. Finally, the unit cells of *planar-based lattices* consist of two-dimensional shapes extruded perpendicular to some surface to make three-dimensional lattices. Technically the honeycomb cores already used in existing aircraft liners can be categorized as a planar-based lattice.

After unit cells have been patterned into a lattice, they can additionally be categorized into two different types: (1) homogeneous or (2) heterogeneous lattices [40]. For *homogeneous lattices*, the unit cells are the same throughout the entire lattice. On the other hand, *heterogeneous lattices* contain unit cells that vary in size, volume fraction, and shape throughout some lattice. An example of some of these different lattice combinations can be seen in Figure 6. A mathematical reference with some of the fundamental equations needed to generate and manipulate these structures can be seen in Appendix A.

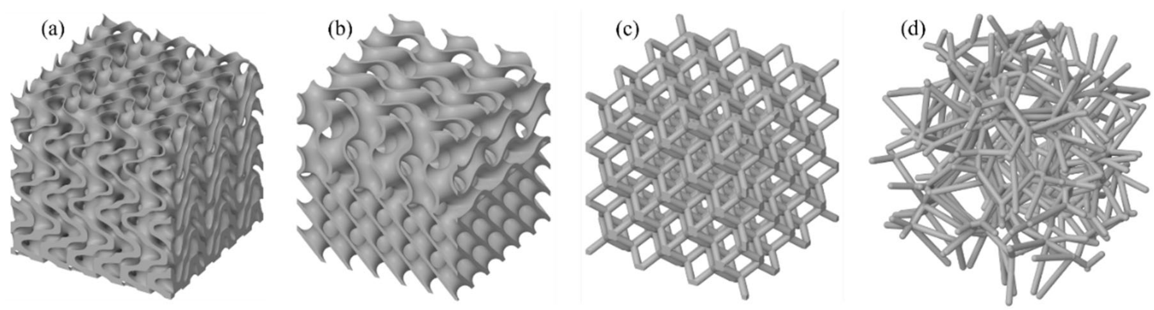

Figure 6. Heterogeneous Fischer-Koch S TPMS lattice with one-dimensional linear volume fraction grading (a), heterogeneous Schwarz D/Gyroid multi-morphology hybrid TPMS lattice with sigmoid transition (b) (adapted from [42], [43]), homogeneous rhombic dodecahedron (also called fluorite) ordered strut-based lattice (c) [39], and Voronoi stochastic strut-based unit cell (d).

Initial research efforts into AM acoustic liners and absorbers have revolved around these lattices and cellular structures, and the TPMS and surface-based lattices have become popular. For example, initial experimental testing on standalone Schwarz P, gyroid, and Schwarz D TPMS structures with various unit cell sizes, volume fractions, and heights made via AM was conducted by Yang et al. [44]. Their testing showed that these lattices have good high-frequency sound absorption potential, which varying unit cell parameters can easily tune. In another study, Winkler et al. [9] proposed using various TPMS structures inside the core of aircraft acoustic liners. By conducting numerical simulations on a Schwarz P TPMS structure inside an SDOF liner, they found good peak and broadband sound attenuation was possible despite a considerable reduction in liner volume. The Schwarz P liner setup used can be seen in Figure 7(a). They also remarked on the tunability and easy parametrization of TPMS structures.

While using well-established unit cells like the TPMS is the most common approach for generating surface-based lattices, developing custom application-specific unit cells is also an option if desired. For example, Deshmukh et al. [45] created three custom surface-based style unit cells by performing boolean operations between solid cubes and spheres arranged in the crystal structure of known metals. The results of these operations for BCC (body-centered cubic), FCC (face-centered cubic), and A15 configurations can be seen Figure 7(b). Standalone testing of lattices using these custom surface-based unit cells showed similar results to the TPMS, where small, lightweight structures achieved both good peak and wideband absorption. These complex lattices are usually only manufacturable with AM, but similar metal foams made through conventional casting processes have also been explored for aircraft engine noise reduction by Jones et al. [46]. In any case, the use of lattices in acoustic absorption applications has not just been limited to surface-based unit cells.

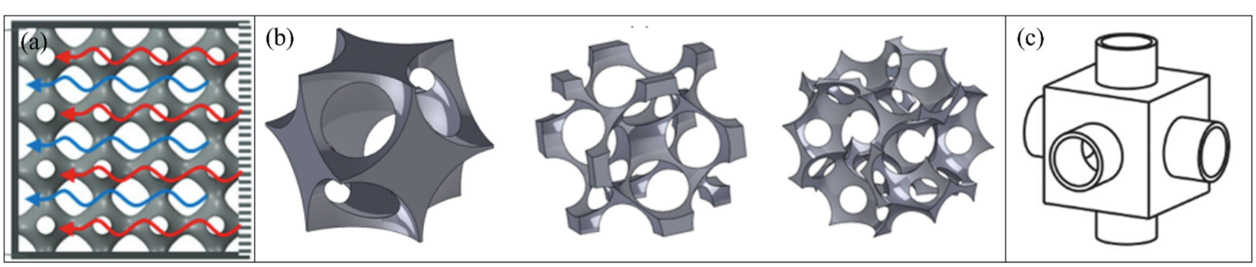

Figure 7. Schwarz P SDOF acoustic liner concept (a) (taken from [9]), custom surface-based style unit cells based on the crystal structure of BCC, FCC, and A15 metals (b) (taken from [45]), and strut-based style unit cells for creating custom acoustic filters (c) (taken from [47]).

No acoustic testing or modeling has been performed to date on any of the commonly used strut-based unit cells, such as the fluorite lattice shown in Figure 6(c). However, a custom strut-based style unit cell, pictured in Figure 7(c), was used by Dingzeyu et al. [47] to make customizable acoustic filters. Furthermore, another study by Johnson and Sharma [48] on fibrous absorbers with a strut-based lattice-like configuration made via AM showed good consistent broadband sound absorption.

Overall, lattices and cellular structures have shown great potential for noise reduction applications due to their excellent energy dissipation, tunable properties, and high strength-to-weight ratio. These examples are only a small selection of how lattices and cellular structures can be used in acoustic absorption applications. Therefore, many more studies and novel lattice-like acoustic metamaterials exist and undoubtedly will continue to be developed in the future using AM technologies.

2.2.2 Designed Structures and Labyrinths

Another approach that has been explored and employed when designing acoustic liners or absorbers for AM is using acoustic labyrinths and custom freeform structures [32], [49]. When used in sound reduction applications, these designed structures and labyrinths aim to guide sound waves such that their energy can be dissipated slowly over time, attenuated by viscous losses/sound-absorbing materials, or terminated by phase cancellation. Some initial research and industrial applications of these designed structures and labyrinths began in the 1930s to make loudspeaker enclosures that improved sound output quality. One famous example of these enclosures would be transmission line speakers, where designed structures and acoustic labyrinths are leveraged to manipulate the back wave produced by a loudspeaker and output it such that it is in phase with the front wave [50]. If done correctly, the resulting output is of better quality and substantially boosted. Unfortunately, designing and manufacturing structures and labyrinths consistently capable of such acoustic tuning is notoriously tricky. However, AM and advanced engineering design tools have been identified and studied as potential solutions for improving the design and manufacturing of these kinds of devices.

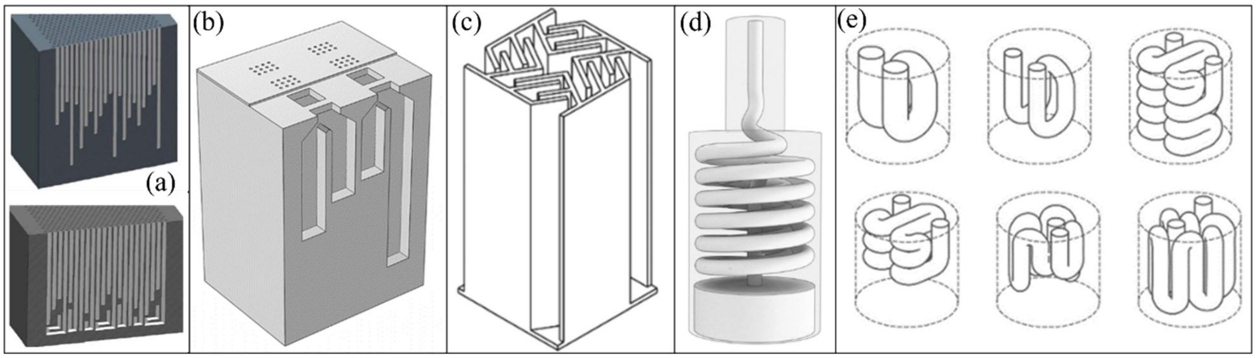

Figure 8. Variable depth acoustic liners (a) (taken from [8]), variable depth acoustic liner with shared inlet ports (b) (taken from [8]), labyrinth acoustic metamaterial (c) (taken from [49]), space coiling Helmholtz resonator (d) (taken from [51]), and various labyrinth designs that produce a passive destructive interface (e) (taken from [49]).

For aircraft acoustic liners, most initial research using designed structures and labyrinths made via AM has revolved around variable-depth liners [32]. *Variable-depth liners* are when the cavity beneath the top surface/facesheet consists of many individual chambers with different sizes, shapes, and lengths. For example, Jones et al. [8] investigated the use of narrow straight and bent chamber variable-depth liners, which are shown in Figure 8(a). One unique aspect of these designs is that the chambers are the same size as typical facesheet perforations, meaning no second facesheet is needed. In addition, they can potentially provide high viscous losses due to their sustained small size. Testing performed on these liners showed tonal absorption behavior at several distinct close frequency values. The same study by Jones et al. also looked at wide-chambered conventional and shared inlet variable-depth liners with customized facesheets (in addition to many other labyrinth-style designs), as pictured in Figure 8(b). Testing performed on these wide chamber samples showed that they could sustain a high level of sound attenuation across a wide frequency range. The customized facesheet is a great way to leverage AM. This fact was also realized in a study by Yang et al. [52] who used AM to make custom facesheets for high-performing multi-DOF empty cavity MPPs.

Designed structures and labyrinths made with AM have also been explored for other acoustic absorption applications outside aircraft acoustic liners. For example, Suárez et al. [49] showcased many labyrinth-style metamaterial surfaces like the one shown in Figure 8(c). Similar to many of the unit cells and lattices previously discussed, they mentioned that these structures have very tunable behavior, making it easy to adapt them to many different scenarios and applications. Other interesting labyrinths that utilized complex networks of tubes and conical spirals, as seen in Figure 8(d) and 8(e), were presented by Suárez et al. [49] and Lechuga et al. [51], respectively. These conical spiral and tube networks allowed for the creation of Helmholtz resonators capable of low-frequency absorption and passive absorbers that worked by creating a destructive interface. These AM-designed structures and acoustic labyrinths are only a small fraction of what has been studied and tested to date. As previously mentioned with the lattices, many more of these novel structures currently exist and will continue to be developed into the future with AM. Software tools to design and optimize these structures are discussed next.

2.2.3 Generative Design and Topology Optimization

Generative design and topology optimization are complex mathematical design algorithms that optimize the layout of material (or negative space) for a component(s) inside a predefined domain based on a set of boundary conditions, constraints, and optimization objectives [53]. While the terms topology optimization and generative design are often used interchangeably, they are not the same. Generally, from a qualitative perspective, an initial volume is defined for topology optimization, and the optimal shape, given the boundary conditions, constraints, and optimization goals, is achieved through material removal. On the other hand, generative design achieves similar outcomes as topology optimization, except instead of removing material to determine the optimal shape, the component is generated or grown like a plant inside a predefined domain. Generative design usually produces a pool of many design variants that users can select from, while topology optimization typically creates a single output based on the underlying optimization algorithm used to eliminate material. The geometry produced by most of these generative design and topology optimization algorithms is very complex, making them a great candidate for AM. An example of a topology-optimized design intended for AM can be seen in Figure 9.

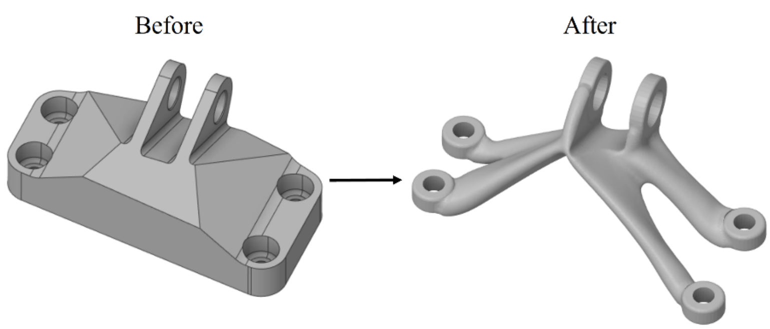

Figure 9. Example of a GE Engine bracket before and after undergoing structural topology optimization [54].

Most initial topology optimization and generative design algorithms and applications have revolved primarily around structural problems like maximizing stiffness or minimizing mass with respect to stress. However, as the popularity of topology optimization and generative design grew, the applications and algorithms expanded to other types of physics. Initially, this included things like heat conduction, fluid flow, and vibrations. More recently, though, preliminary research has been conducted on how generative design and topology optimization can be leveraged in acoustic and aeroacoustic applications.

No research focusing specifically on acoustic liner design with topology optimization or generative design has been performed to date. This is not the case for other types of acoustic absorbers, however, many of which could be adapted for aircraft acoustic liners. For example, Azevedo et al. [55] investigated how topology optimization could be used to create internal muffler structures that produced a high transmission loss, as seen in Figure 10(a). The transmission loss is a way to characterize the reduction in the magnitude of some signal characteristic between two points [3]. Chen et al. [56] conducted a comparable study, looking at topology-optimized mufflers and aircraft bodies, as shown in Figure 10(b). However, instead of determining an internal structure, the approach by Chen et al. determined the optimal layout of multiple sound-absorbing materials inside a given volume.

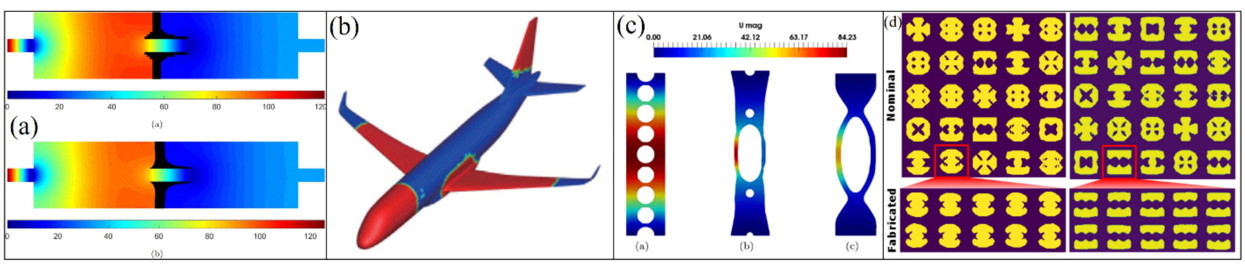

Figure 10. Topology-optimized muffler that maximized transmission loss (a) (taken from [55]), the optimal layout of multiple sound absorbing materials in an aircraft body determined with topology optimization (b) (taken from [56]), a compliant mechanical-acoustic device designed with topology optimization for noise reduction in a duct (c) (taken from [57]), and acoustic absorbing hole shapes created with generative design (d) (taken from [58]).

Another study with similar objectives by Dilgen et al. [57] researched using directly coupled mechanical-acoustic multiphysics topology optimization to design compliant membrane absorbers for ducts, as seen in Figure 10(c). Despite their differences, these different topology optimization approaches demonstrated that they were all practical approaches to designing these acoustic absorbers. Alternatively, Wei et al. [58] took a different approach where generative design was used to create novel planar orifice shapes with good acoustic absorption potential, as seen in Figure 10(d). Similarly, Kook and Jensen [59] also looked at making sound-absorbing holes with topology optimization instead of generative design. These planar orifice designs make excellent candidates for AM aircraft acoustic liner facesheets. Research and software development in this area is still in the beginning stages; so, growth is expected going forward.

2.3 Review of Design and Development Methods for Acoustic Liners

Methods to design aircraft acoustic liners have been well-established and applied throughout the aerospace industry. Generally, this process can be broken down into three separate sequential steps with a feedback loop connecting the first and last stages [9]. Initially, an inverse optimization study is performed using a predefined target for one or more key acoustic liner QOIs (acoustic impedance, weight, cost, etc.) to find liner design configurations that closely or exactly match the target QOIs. Next, the performance of the optimized liner designs are evaluated at the engine level to see how well the noise is attenuated in the engine duct and far field. Ultimately, the system-level impacts of the proposed liner designs are determined to verify that requirements and regulations are being satisfied. Lastly, a final design selection can be made based on the observations and data collected for the various liners. However, if no candidate designs are ready for final selection, the design loop can be completed again with updated target QOIs. The performance evaluations completed during the various steps are typically carried out using either physics-based modeling, numerical simulations, or empirical testing (or some combination). An example of the acoustic liner design methodology used by Collins Aerospace, which generally represents the industry as a whole, can be seen in Figure 11.

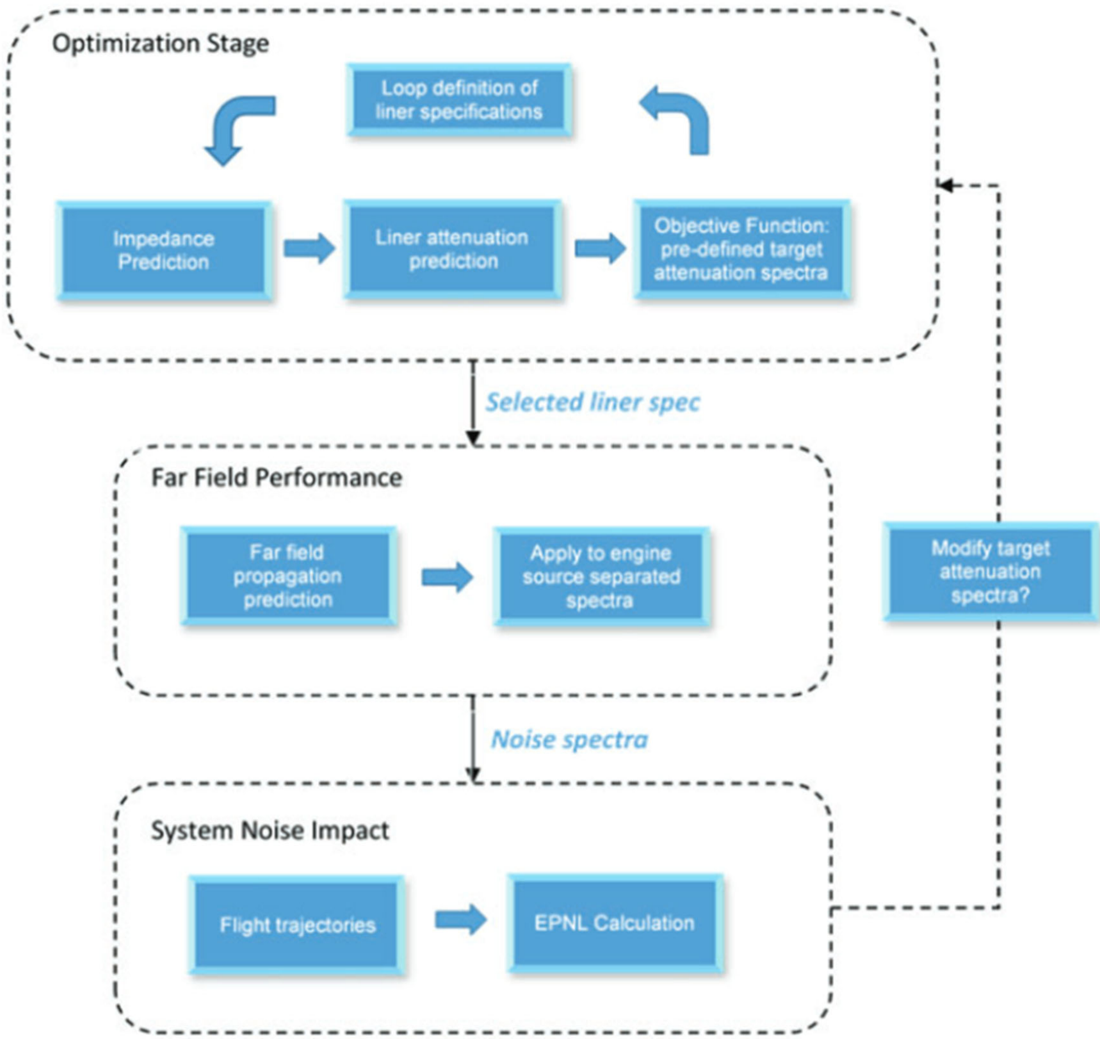

Figure 11. Acoustic liner design and development method at Collins Aerospace (taken from [9]).

The design and development method shown in Figure 11 works well and has successfully optimized many liner designs. It can potentially cause some challenges, though, when the initial target QOIs are determined with simplified models, unknowns, and uncertainties. A similar issue can also arise with the performance evaluation techniques used during each step. Under these circumstances, an optimal solution can still be achieved mathematically. However, the selected designs often do not perform as expected due to high sensitivities in things like design parameters, manufacturing tolerances, and differences in environmental conditions [60].

Therefore, in the slightly adjusted workflow shown in Figure 12, the target QOI determination and liner performance evaluation processes leverage a nested statistical pseudorandom sampling approach to perform optimization under uncertainty (OUU). Performing OUU is beneficial because it allows for active design optimization while accounting for uncertainty. While performing OUU is more challenging and time-consuming, the resulting solutions are usually much more robust.

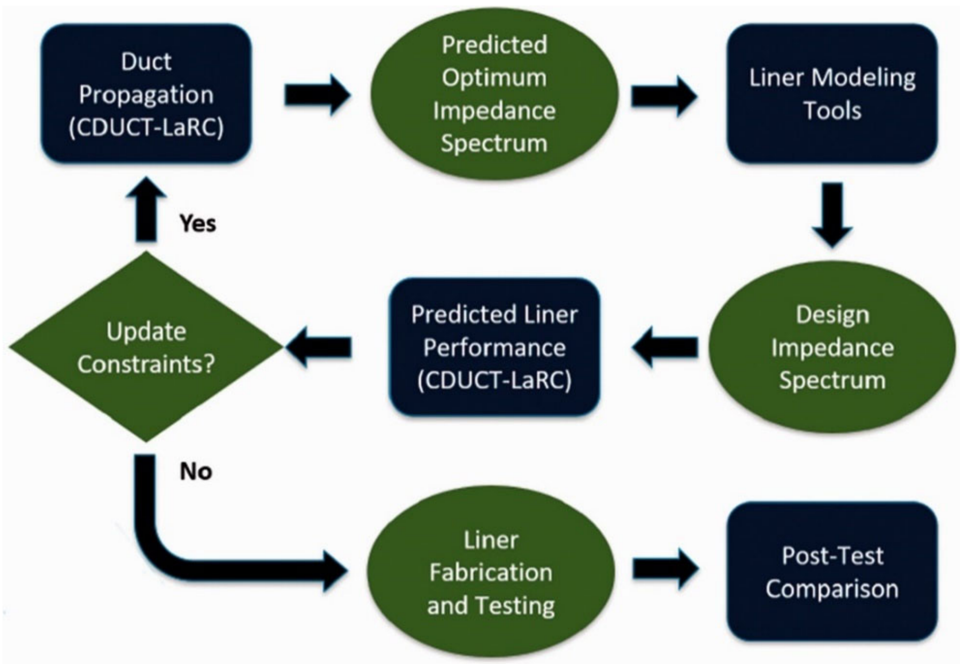

Figure 12. Acoustic liner development workflow considering uncertainty (taken from [61]).

Both of these design methods implement an indirect liner optimization approach, where a liner design is optimized to match one or more specific target QOIs determined through a separate optimization process and then evaluated at the system level. This is in contrast to the direct liner optimization approach, where one or more acoustic liner performance QOIs are maximized or minimized in a general sense [61].

This chapter presents a literature review going over introductory background information on acoustic liners, current research on conventional and AM liners/sound absorbers, and development methods for aircraft acoustic liners. Overall, the main takeaway is that the honeycomb core liners currently seeing widespread use in many aircraft are expected to struggle to meet the weight, size, and attenuation requirements of future high-bypass ratio turbofan engines. Therefore, new high-performance acoustic liners potentially using recently proposed concepts, such as lattice structures, must be developed to address this issue. Chapter 3 proposes a new AM-focused design and development methodology that possibly enables these new concepts by addressing the design concept generation and manufacturing shortcomings of existing workflows. These additional design and manufacturing aspects could be crucial for successfully implementing the next generation of AM aircraft acoustic liners.

Chapter 3

Design and Development Method

In this chapter, the information, learnings, and insights from the literature review in Chapter 2 are leveraged to propose a new AM-focused design and development method that expands on the approaches in Figures 11 and 12 to include detailed design and manufacturing steps. This new five-step design and development process is presented and explained at the beginning of this chapter. Then, throughout the remainder of this chapter, the specific details that make up each individual step are discussed.

3.1 Proposed Design and Development Method

The methods discussed in the previous chapter are both data-driven iterative workflows that include the critical areas of modeling, simulation, optimization, and testing that are needed to design and develop conventional acoustic liners properly. However, they do not include much detail about design concept generation and manufacturing. These aspects could be crucial for successfully designing and developing AM liners that meet noise attenuation, size, and weight requirements.

To address this gap, a new AM-focused acoustic liner design and development method that combines these new aspects with the concepts already found in the existing workflows is proposed in Figure 13. The main difference between the AM-focused workflow and the existing ones is that it is a direct optimization approach instead of an indirect one. Overall, the new AM-focused development workflow consists of five phases which are grouped by color in Figure 13 and explained in the remainder of this chapter.

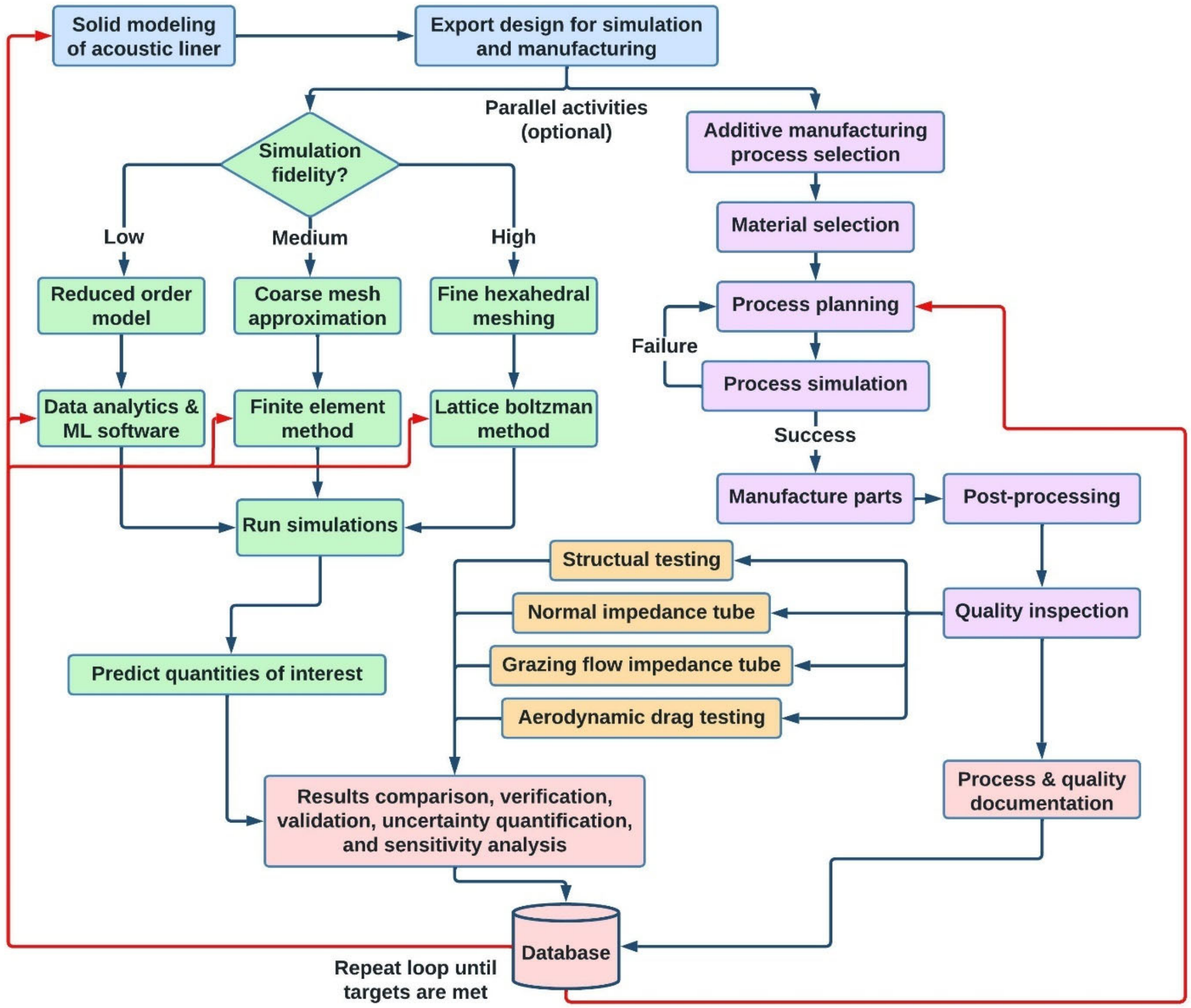

Figure 13. Proposed method to design and develop AM acoustic liners.

The first step (highlighted in blue) is the design concept generation and solid modeling phase. This step must be completed before moving forward because the 3D model data generated here is required to start the next steps. Once completed, the workflow comes to a junction where two different branches become available. One branch contains all of the modeling and simulation activities (highlighted in green). The other branch contains two activities: (1) manufacturing and (2) quality inspection (highlighted in purple), followed by physical testing of the newly manufactured samples (highlighted in orange). Both of these branches can be completed in parallel if chosen, which is enabled by AM's ability to create high-fidelity prototypes rapidly.

Only completing one branch is required to be able to do an entire workflow iteration. For example, if working with a new design, both branches may want to be completed so that the manufacturing and testing data can be used to verify, validate, and calibrate the modeling and simulation tools. If trying to optimize the dimensions of an established design configuration, though, only one branch might be used to save time and reduce costs. Ideally, if completing both branches, they would be done in parallel by different teams/individuals who just focus on one branch so that cycle times can be reduced.

Both branches lead to the final step, which is the database development and optimization phase (highlighted in red). During this last step, all of the information and data generated in the previous steps are logged in a central database with optimization feedback loops leading into several previous steps. This feedback data is used to help drive future iterations. This process can be repeated until the desired results are achieved. All of these steps have many substeps and options available, which are discussed in more detail next.

3.2 Solid Modeling

The first step in the AM acoustic liner development workflow (highlighted in light blue) is to use computer-aided design (CAD) software to create a 3D solid model of the concept of interest. Depending on the design complexity, 3D solid modeling can be one of the trickiest yet most important steps. A significant amount of the modeling challenges stem from the limited degree of complexity that most current primitive and parametric CAD software packages can handle. Some examples of popular commercial parametric CAD programs include Dassault

Systemes Solidworks[1], Autodesk Inventor[2], and PTC Creo[3]. Most primitive and parametric CAD software uses boundary representation (B-rep) data to define a solid model. B-rep can represent these three-dimensional solid models by defining parametric mathematical relationships between many geometric objects like regions, surfaces, edges, and vertices. While B-rep is a precise way to model decently complex objects, it can start to break down and become too computationally expensive when designing objects like lattices for AM.

A few implicit modeling software programs have been developed to address this AM design shortcoming with traditional CAD. Commercial software examples would include nTopology's nTop[4] and Altair Engineering's Gen3D[5]. Implicit modeling represents objects with implicit signed scalar fields instead of B-rep data. The implicit approach is much more computationally efficient, allowing for additional complexity and control when modeling. Therefore, implicit modeling software might need to be used when designing acoustic liners that utilize complex structures.

It is generally better to use traditional CAD over implicit modeling when feasible, though, as it is more numerically precise and easier to transfer to downstream steps. If implicit modeling software is needed, then primitive and parametric CAD can be used beforehand to create envelopes from which the structures are generated. Finally, the design can be exported into whatever formats are required for the proceeding steps. Since the conversion of implicit data to B-rep formats is challenging to calculate, memory intensive, and can cause significant losses in fidelity, mesh-based geometry (MBG) that uses many triangular facets to define the surface of

---

[1] https://www.solidworks.com/
[2] https://www.autodesk.com/products/inventor/overview
[3] https://www.ptc.com/en/products/creo
[4] https://ntopology.com/
[5] https://gen3d.com/

a geometry is usually used instead. Standard MBG file types include the stereolithography format (.stl), additive manufacturing format (.amf), and 3D manufacturing format (.3mf).

3.3 Test Sample Manufacturing and Quality Inspection

3.3.1 Manufacturing and Post-Processing

Test sample manufacturing can begin once the exported design files from the first step are received (assuming this branch is not being skipped). The process starts by selecting one or more of the seven types of AM processes and a compatible material to fabricate the acoustic liner prototypes. Each of the different AM process types and its accompanying materials has its own set of unique properties, characteristics, and advantages/disadvantages relative to the others. Table 1 briefly summarizes the different AM process types, some defining characteristics, and the common materials used in each. Ultimately, the setup that should be employed to make the samples depends on many factors. However, selecting various process types, materials, machines, and settings to make a set of samples can help characterize their impact on the performance and determine what works best.

Table 1. Table summarizing the seven types of AM processes according to ASTM standard 52900 (taken from [10]), some notable process characteristics (adapted from [62]), and common compatible materials for each (taken from [63]).

AM Process Type	**ASTM Standard 52900 Description** [10]	**Characteristics**	**Materials** [63]
Binder jetting (BJT)	"additive manufacturing process in which a liquid bonding agent is selectively deposited to join powder materials."	-Able to make precise high-resolution complex parts -Large build chamber and fast printing allows for high production rates -Infiltration and sintering can cause component shrinkage -Lower mechanical properties than other AM processes	"Powdered plastic, metal, ceramics, glass, and sand"
Directed energy deposition (DED)	"additive manufacturing process in which focused thermal energy is used to fuse materials by melting as they are being deposited."	-Large build volumes and high material deposition rates allow for big parts to be made quickly -Able to make multi-material components from a wide array of material choices -Initial machine procurement and setup can be expensive and time-consuming -Poor geometric resolution often makes post-processing required	"Metal wire and powder, with ceramics"
Material extrusion (MEX)	"additive manufacturing process in which material is selectively dispensed through a nozzle or orifice."	-Entry-level machines and materials are more affordable than other process types -A bunch of different material options are available and do not require much post-processing -Parts tend to have lower accuracy and higher surface roughnesses -Significant warping and shrinkage can occur during a build	"Thermoplastic filaments and pellets; liquids and slurries"
Material jetting (MJT)	"additive manufacturing process in which droplets of feedstock material are selectively deposited."	-Able to make complex parts with high-resolution features with a good amount of accuracy -High-tolerance values and smooth surface finishes are common -Long print times because of the droplet deposition process -Parts have poor structural properties and fail in a brittle manor	"Photopolymers, polymers, waxes"
Powder bed fusion (PBF)	"additive manufacturing process in which thermal energy selectively fuses regions of a powder bed."	-Able to make strong, complex parts with high-tolerance values -No support structures are needed for printing polymer materials -Long printing and post-processing times are usually required -Materials are expensive and prone to distortion from thermal gradients	"Plastics, metal and ceramic powders, and sand"
Sheet lamination (SHL)	"Additive manufacturing process in which sheets of material are bonded to form a part."	-Able to build large parts without the use of support structures -Able to print multi-material and multi-color parts out of safe and inexpensive materials -Not able to handle making parts with complex shapes and internal features -Debonding of sheet layers can occur over time	"Paper, plastic sheets, and metal foils/tapes"
Vat photopolymerization (VPP)	"additive manufacturing process in which liquid photopolymer in a vat is selectively cured by light-activated polymerization."	-Able to make complex parts with high-resolution features and a smooth surface finish -One of the fastest printing methods -Materials are limited in selection and can be expensive -Post-processing can take a long time and be messy	"UV-Curable photopolymer resins"

For the frequency range of interest, the difference in the absorption coefficient between a solid metal and a hard plastic sheet is negligible. This approximation holds up well until SPL levels are high enough that the acoustic loading force can start to cause vibrations in the structure of the liner (mainly at the facesheet). In this scenario, the retroactive effect between the mechanical and acoustic fields is not negligible. This can lead to different acoustic behavior of samples made from different materials, even if they are the same design. Consequently, besides this exception, plastic materials can be used to prototype liners throughout this workflow, even though they will probably ultimately be made from a lightweight metallic or ceramic material. Plastic materials are preferred because they are significantly less expensive, more accessible, and easier to work with than metals.

The primary AM process types of interest in acoustic liner prototyping are thus VPP and MJT because they can directly print complex plastic samples with high-tolerances and high-resolution features. MEX is also a potential option, but it would have trouble consistently making the required sub-millimeter features. While PBF and BTJ can also work with plastic materials and likely make the needed geometries, they are more expensive, making their use less favorable. Ultimately, towards the end of the development process, switching to the end-use lightweight metallic material would be best when converging toward a final design. This would allow for testing and evaluation of a full-specification part in addition to seeing how the new material and manufacturing process compares to the previous prototypes. PBF is the leading candidate for additively manufacturing metal acoustic liner samples because it can create complex geometries with high-tolerances out of aluminum, titanium, or nickel-based alloys that have the required thermal and structural properties. However, in the future, this could change. For example, a better approach could be using a hybrid AM process like DED combined with a five-axis CNC mill to print the liners directly into a nacelle. As of right now, this is definitely not the situation, however.

Once one or more AM process types and accompanying materials have been selected, a process plan outlining the manufacturing details is created. In this case, the process planning consists of figuring out the best way to fabricate the parts layer-by-layer and then translating that into a program the printers can execute. For this workflow, the process planning begins by taking the MBG files created during the 3D solid modeling phase and checking them for defects and dimensional inaccuracies. If needed, several CAD programs contain MBG tools that can be used to repair and refine them.

Next, the clean geometry file is imported into a build preparation software program, also frequently referred to as a slicer. The purpose of the slicer is to generate the machine code needed to print the part from a given geometry file in addition to potentially hundreds of other inputs (most of which are already preset). The manufacturer often provides the slicer software when a machine is purchased, but several different open-source options, like Ultimaker Cura[6] for MEX machines, are also available. Typically it is best to stick with the slicer program the manufacturer recommends and maintains for a given machine.

The other inputs besides the geometry file vary depending on things like the AM process type, machine manufacturer, and slicer software. However, most have a few critical high-impact inputs in common. One of the first is determining the liner's orientation and position relative to the substrate and other nearby parts. Ideally, all parts would be oriented and nested together to optimize things like build time, material usage, the volume/contact area of support structures,

[6] https://ultimaker.com/software/ultimaker-cura

and resulting material quality. Obtaining the optimized layout can be difficult and time-consuming, but many slicers have automated functions that can help streamline the process.

After a suitable orientation and nesting is achieved, the machine process parameters must be configured inside the slicer program. Standard input parameters would include settings like layer height, print speed, laser power, extrusion temperature, and infill/scan pattern. A good place to start is usually using the process parameters recommended by the machine manufacturer. If interested, the effect of these different process parameter inputs can be experimentally investigated to determine what works best. Finally, after setting the process settings, the machine code can be generated and uploaded to the printer.

Occasionally build failures occur while components are being printed for reasons ranging from distortion to unsupported features. Sometimes these failures are just one-off events, but the underlying process configuration is often responsible. Regardless, AM build failures cause increased costs, longer lead times, and material/energy waste, so they should try to be avoided as much as possible [64]. AM process simulation is one emerging tool that can help prevent build failures before they happen [65]. These simulations can be complicated multiphysics finite element simulations for AM processes using metallic materials like PBF, DED, and BJT [66]–[68]. When working with polymers and more straightforward processes, the simulation would be just a detailed animation/visualization of the entire build, ensuring everything looks correct. Therefore, before starting any print job, it is recommended that some form of AM process simulation be run to verify the build setup and reduce the odds of failure. If the simulation results show a successful build, then the print job can be started (assuming the machines are calibrated); otherwise, the process planning phase should be reevaluated until the issues are fixed. One important thing to note during this phase is that all the data generated and steps taken should be well-documented so that they can be committed to the database at the end of the workflow.

After the liner prototype print jobs finish, samples must undergo a few post-processing steps to get them ready for testing. Like many preceding steps, the exact post-processing procedure varies depending on the AM process. Generally, the first action is to remove the components from the build plate. For polymers, this is typically done purely by hand or using simple hand tools like paint scrapers and clippers. The parts for metal builds can be removed using one or more cutting processes, such as bandsawing, electrical discharge machining (EDM), or CNC milling, after stress relief is performed on the parts to reduce residual stresses that often build up in metal AM processes.

Once the components are freed, attention should be directed to removing support structures and excess feedstock material. Any rough surfaces present can also be addressed here. In particular, rough surfaces where the support structures contact the AM part are common. Removal of support structures and excess material can be done with the same methods used during build plate separation. In addition, techniques like grinding, sanding, barrel tumbling, immersion in a solvent excited with ultrasonic waves or a magnetic stir rod, and compressed air guns may also be helpful. If trying to print fully consolidated liners, removing support structures and excess material through facesheet holes alone can be challenging, if not impossible. Getting the access needed to remove supports and excess material usually requires printing the acoustic liner in multiple components and assembling them after post-processing is complete. The easiest way to get around this is by separately printing the backplate and main section. This is not ideal, though, because it takes away one of AM's most significant strengths of assembly consolidation. Also, performance-reducing acoustic leakage can occur if not appropriately sealed during assembly. Before assembly, after supports and excess material have already been removed, additional post-processing steps are sometimes required to finish parts. For example, sintering and infiltration are needed for parts made with BJT, or UV light curing is used to harden samples made with VPP and MJT. Documentation about the post-processing approach and steps should also be recorded so that it can be added to the shared database.

3.3.2 Quality Inspection

Prior to sending the completed liner samples off for physical testing, some QOIs of the newly manufactured components should be assessed to see how they turned out. Since the performance of acoustic liners is primarily driven by their shape and size, most of the quality inspection revolves around quantifying how close the actual and nominal CAD geometry match up. Also, other inspection techniques that characterize the quality of AM materials and detect commonly occurring defects are of interest here as well. All of the data generated during these evaluations are documented and added to the central database, which helps improve liner design, sample manufacturing, and the accuracy of modeling and simulation in future iterations. A few nondestructive and destructive inspection techniques that determine the desired QOIs for these acoustic liner samples are discussed in more detail next.

3.3.2.1 Computed Tomography

Computed tomography (CT) is a nondestructive evaluation technique that can create two and three-dimensional cross-sectional images of a sample [69]. By analyzing these pictures with image analysis software or converting them into a CAD file, the dimensions/shapes of the scanned objects can be measured. Since the entire volume is visible, detection of internal defects is also possible. For example, a geometry comparison between a nominal acoustic liner facesheet and a scanned facesheet sample made with VPP can be seen in Figure 14.

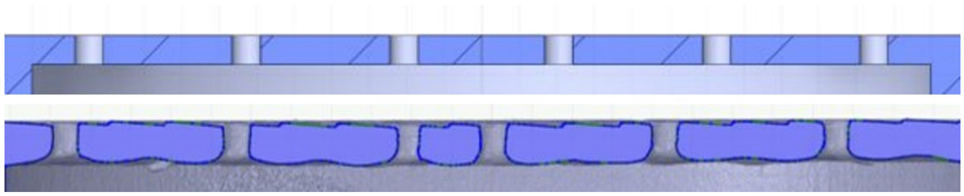

Figure 14. Comparison of scanned acoustic liner facesheet made with VPP and nominal CAD geometry. Scan data courtesy of the Raytheon Technologies Research Center.

While the wider-scale application of CT in manufacturing inspection is relatively recent, it has been leveraged for medical imaging for many years. The general CT setup usually consists of some sample on a turntable between an X-ray generator and a digital detector that measures radiation intensity. As the turntable rotates in many small discrete steps, an X-ray beam passes through the sample, and the digital detector records the resulting radiation intensity distribution for each projection. After the number of specified steps is complete, computer algorithms are used to stitch all of the individual intensity distributions into the final output images [70].

The image data obtained from x-ray CT scans could be helpful in many different areas of the AM acoustic liner development workflow. For example, in Figure 14, it was observed that the printed facesheet hole diameters were smaller than the nominal CAD diameter. Therefore, the manufacturing process parameters were adjusted to minimize this hole shrinkage in future prints. Alternatively, if different process settings had not fixed the issue, then the diameter differences can be used to calculate a design correction value that could be implemented in the nominal CAD file to account for this.

Another observation of the comparison in Figure 14 is the rounded hole edges present in the printed sample. For example, if trying to compare physical testing and simulation results, the x-ray CT geometry file with the rounded edges could be used as the basis for the simulation mesh instead of the nominal geometry to increase accuracy and comparability. Ultimately, while x-ray CT provides high-fidelity data covering many of the desired QOIs, it is too expensive and time-consuming to use regularly. However, leveraging x-ray CT occasionally for new sample designs or after significant changes could be a good approach.

3.3.2.2 Optical 3D Scanning

Optical 3D scanning is a nondestructive evaluation technique that can characterize the dimensions and shapes of a physical sample. Some commonly used optical 3D scanning approaches include the time-of-flight, triangulation, ranging, interferometry, and structured light scanning methods [71]. These methods collect a series of points in 3D space known as a point cloud. Then using the point cloud data, a faceted surface representing that of the scanned sample can be constructed and made into a CAD file for comparisons to the nominal geometry. While optical 3D scanning can create accurate and high-resolution surfaces decently quickly, it has one major drawback. Unlike x-ray CT, optical 3D scanning cannot collect data on surfaces without a direct line of sight from the outside. Therefore, only the dimensions and shape of the backplate, outside core walls, and top surface of the facesheet could be obtained for most acoustic liner samples. Depending on what exact dimensions and shapes are of interest, this may or may not be a good technique to use.

3.3.2.3 Optical Profilometry

Optical profilometry is a nondestructive surface metrology technique that can be used to characterize the dimensions and surface roughness of an acoustic liner facesheet. Also, surface defects like cracks, balling, and semi-melted powder that can occur during AM processes can be detected as well. There are a few different optical profilometry methods, like focus variation, white light interferometry, and laser scanning confocal [72].

At a basic level, all of these different optical profilometry techniques manipulate light in some way to measure a surface and create a 3D model or image of it. The main difference between these techniques is the resolution of the measurements they can make at some given length scale [72]. Typically, these measurements are made at length scales ranging from just a few nanometers up to a couple of millimeters or more. An example of some optical profilometry scans using a Zygo NexView3D for an acoustic liner facesheet made with VPP can be seen in Figure 15.

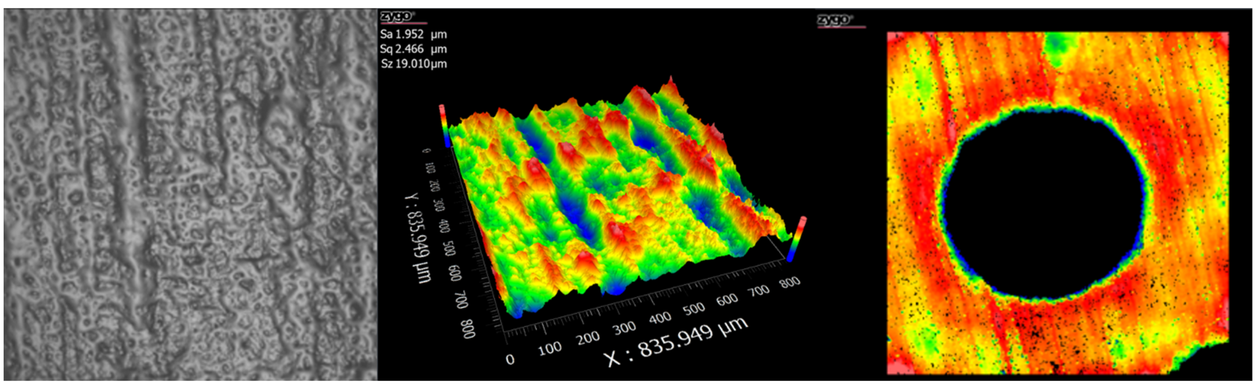

Figure 15. Optical profilometry scans to determine surface roughness and hole shape of an acoustic liner facesheet manufactured with VPP. To provide a sense of scale, the nominal diameter of the hole pictured above is 0.762 mm.

As jet fuel costs continue to rise, there is significant interest in finding ways to reduce the drag produced by acoustic liners [73]. Most of the drag a liner creates is caused by the acoustic liner surface roughness (considering both holes and the facesheet surface as the total roughness). Therefore, optical profilometry scans could be a good approach to quantifying and optimizing the acoustic liner manufacturing process to minimize drag or other QOIs. The pictures in Figure 15 are just a measurement at a single point, but it is possible to take many measurements and stitch them together to get a complete model of the facesheet. In addition to the surface roughness, the shape morphology and dimensions of the facesheet holes could also be characterized.

3.3.2.4 Image Analysis

One thing that x-ray CT, optical 3D scanning, and optical profilometry evaluation techniques have in common is that the data collection and processing are labor-intensive, time-consuming, and expensive. Therefore, using these methods to evaluate the dimensions and shape of several liner samples would not be very practical. One high throughput technique that can be used to rapidly evaluate acoustic liner facesheet dimensions and shapes (holes in particular) is image analysis. Image analysis refers to the process of taking a picture and loading it into a software program that can extract many different types of information from it. Examples of these outputs when analyzing a facesheet's dimensions and shapes would include things like average hole diameter, area, circularity, aspect ratio, and total length/width [74]. Since both the initial picture and analysis of it are carried out using a computer, there is potential to automate this process. A fully automated image analysis process would allow for rapid measurement of many acoustic liner samples.

3.3.2.5 Double Active Transient Thermography

So far, the only evaluation technique discussed that can detect internal defects is x-ray CT scanning. However, a much cheaper and more efficient approach capable of doing this would be highly desirable. One potential nondestructive evaluation technique that could be used to detect internal defects in facesheets is double-active transient thermography (DATT) [75]. DATT works by applying a radiation heat source to one side of an object while a cold source is applied to another surface, creating a thermal gradient in the material. Using a thermal camera to watch the evolution of the temperature field over time could allow for internal defects to be spotted. An example of how internal defects were spotted for an AM component using DATT nondestructive evaluation can be seen in Figure 16.

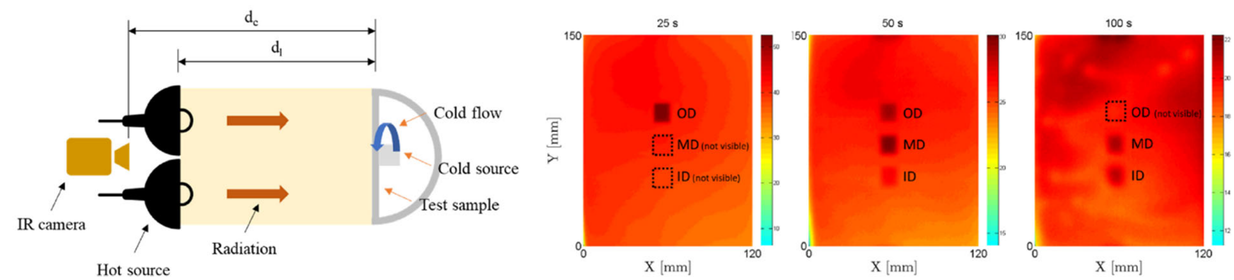

Figure 16. Example of DATT experimental layout and how the evolution of the temperature field over time can show internal defects (taken from [75]).

3.3.2.6 Leak or Pressure Testing

For an acoustic liner to perform at its best, the cavity between the facesheet and backplate must be fully sealed. A fully sealed liner would only allow for flow in and out of the facesheet holes. If the cavity is not fully sealed, acoustic leakage can occur at interfaces between the different parts. Acoustic leakage can significantly reduce the performance of a liner. AM has the potential to solve this issue by combining the facesheet, core section, and backplate into a single part with no interfaces for leakage to occur. However, as previously mentioned, removing the excess material and support structures through the facesheet is challenging, requiring AM liners to be printed in multiple pieces and assembled after post-processing.

There are a few standard methods to test for leakage in acoustic devices, but they are not applied here; instead, a few simple tests can be devised to evaluate this for aircraft acoustic liners specifically. One example would be to place a liner sample on a clean, dry cloth or paper towel, fill the cavity with water, and wait a few minutes to see if the cloth or paper towel is wet. If not, that could mean that the cavity has a good seal. This is just one idea, but this could be done in a whole range of ways.

3.3.2.7 Material Test Artifacts

One common practice in AM when the material quality of one or more components needs to be determined without destructively testing the main part is to additively manufacture test artifacts along with the component. A test artifact's purpose is to evaluate an AM process's performance. If a test artifact printed next to a part showed good properties, then it would infer that everything else built with it would show similar qualities. Some common AM test artifact examples would include things like tensile test specimens, Charpy impact bars, and density cubes, to name a few. These test artifacts could be helpful for the structural and material quality evaluation of acoustic liner samples.

3.4 Physical Testing

Once the prototypes have finished manufacturing and quality inspection, they are ready for physical testing. There are four primary areas where the performance of acoustic liners can be experimentally characterized: acoustic, aeroacoustic, aerodynamic, and structural.

3.4.1 Normal Incidence Impedance Tube

As previously mentioned, acoustic impedance and absorption coefficient are among the most critical acoustic liner performance QOIs. One of the recommended ways to experimentally determine acoustic impedance for a liner sample is to use the two-microphone normal impedance tube (NIT) testing method described in ASTM standard E1050 [73], [76]. This standard calls for one or more sound sources (loudspeakers/compression drivers) to be fixed to one end of a waveguide with either a round or square cross-section across from a test sample at the other end. The NIT usually has a breakpoint somewhere in the waveguide so that samples can be inserted/removed and sealed inside. A short distance from the test sample is two closely placed microphones that sit flush with the top inside surface. Optionally, an additional third microphone can be placed directly above the sample facesheet to measure SPL levels at the top surface.

The microphones are attached to a data acquisition module (DAQ) that translates the analog acoustic pressure signals into digital signals and sends them to a connected computer. This computer is also wired to an amplifier that powers and controls the compression driver. An example of an NIT setup minus the DAQ, computer, and amplifier can be seen in Figure 17. Typically, either a broadband white noise, controlled-amplitude linear swept sine, or stepped sine sound source signals are used [73]. After the sample has been placed in the tube and the electronics wired up, the testing process can begin. Testing starts when one of the transient sound signals is played through the compression driver at some predetermined SPL; during this entire period, all the microphones are recording acoustic pressure values. The process of calculating the acoustic liner QOIs from this transient data is described next [76].

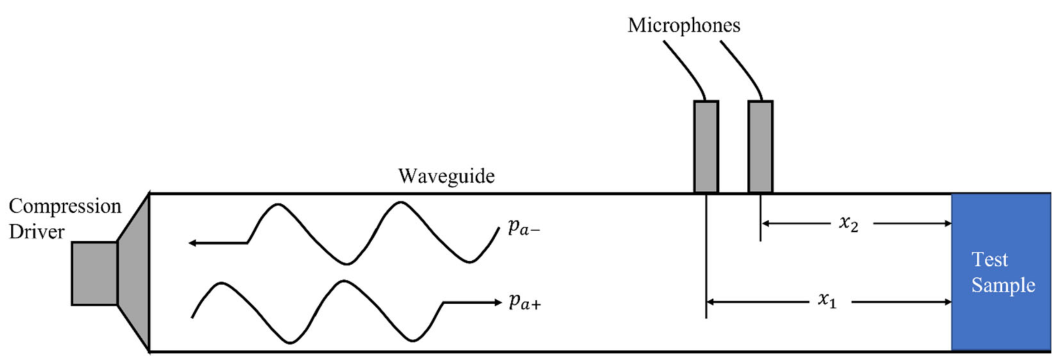

Figure 17. Diagram of a typical NIT using the two-microphone method. The computer, DAQ, and amplifier components are not shown.

The two-microphone NIT testing method is known as an “impedance eduction” approach because the acoustic impedance is not directly measured; instead, it is based on acoustic pressure measurements. Therefore, the first step in translating these acoustic pressure values into acoustic impedance (in addition to other QOIs) is to understand the acoustic pressure as a function of waveguide position assuming a plane wave, as shown in Equation 5 [3].

$$p_a(x) = p_{a+}\, e^{-jkx} + p_{a-}\, e^{jkx} \tag{5}$$

Instead of referencing acoustic pressure values, it is common to translate the root mean square (RMS) of acoustic pressure to the logarithmic decibel (dB) scale relative to some reference acoustic pressure value ($20\ \mu p_a$ for atmospheric air) using Equation 6 [3], [77]. Decibels make visualization and interpretation of acoustic pressure values that span a wide range of magnitude orders easier. All downstream calculations should use the original acoustic pressure values instead of the SPL.

$$SPL = 20\ \log_{10}\left(\frac{p_{a,RMS}}{p_{ref}}\right) \tag{6}$$

Calculating the acoustic pressure RMS depends on whether acoustic pressure is measured in the frequency or time domain. The equations to calculate the RMS acoustic pressure for each domain type, respectively, are given by Equations 7 and 8 [3], [77].

$$p_{a,RMS} = \sqrt{\frac{1}{2}\, p_a\, \overline{p_a}} \qquad p_{a,RMS} = \sqrt{\frac{1}{\Delta t}\int_{t_1}^{t_2} p_a^2(t)\, dt} \tag{7,8}$$

Next, a complex transfer function must be determined between the two microphones mounted on the top surface. In this case, the transfer function between the two microphones is just the ratio of complex acoustic pressure at microphone two to the complex acoustic pressure at microphone one, as shown in Equation 9 [76]. In the frequency domain, this ratio can be directly evaluated, but this cannot be directly found in the time domain; so, it must be approximated numerically using a technique like Welch's averaged periodogram method instead [76].

$$H_{12} = \frac{p_{a2}}{p_{a1}} = \frac{p_{a+}\, e^{-jkx_2} + p_{a-}\, e^{jkx_2}}{p_{a+}\, e^{-jkx_1} + p_{a-}\, e^{jkx_1}} \tag{9}$$

Simplifications can be made to Equation 9 by plugging in Equations 10-12. Equation 10 represents the transfer function of the incident wave from the test sample, Equation 11 represents the transfer function of the reflected wave from the test sample, and Equation 12 represents the reflection [76].

$$H_h = e^{-jkx_2} \qquad H_r = e^{jkx_1} \qquad R = \frac{p_{a-}}{p_{a+}} \tag{10,11,12}$$

The result of plugging Equations 10-12 into Equation 9 and solving for the reflection is given by Equation 13 [76]. Equation 13 finally gives the direct relationship between the microphone acoustic pressure measurements and a performance QOI.

$$R = \frac{H_{12} - H_h}{H_r - H_{12}}\, e^{j2kx_1} \tag{13}$$

Using the reflection values found with Equation 13, the specific acoustic impedance can be calculated using Equation 14 [76]. The difference between acoustic impedance and specific acoustic impedance is that it is normalized relative to the product of the speed of sound and density. Similar to acoustic impedance, specific acoustic impedance's real and imaginary components are known as specific resistance and specific reactance, respectively.

$$Z_{\rho c} = \frac{Z}{\rho c} = \frac{1 + R}{1 - R} \tag{14}$$

Equation 15 can calculate the sample's normal incidence sound absorption coefficient using the reflection values found in Equation 13 [76]. Alternatively, the sound absorption coefficient can be calculated with the specific acoustic impedance values found with Equation 14 using Equation 4. Both methods yield the same answer.

$$\alpha = 1 - |R|^2 \tag{15}$$

Another way to look at the sound absorption behavior is using sound attenuation. Sound attenuation describes the reduction in amplitude of a single-frequency plane wave per unit length. The sound attenuation on the dB scale can be calculated from the absorption coefficient using Equation 16 [3], [9].

$$\mu = -10\ \log_{10}(1 - \alpha) \tag{16}$$

The acoustic liner performance QOIs determined with the two microphone NIT testing method are only valid for a particular frequency range that depends on microphone spacing, waveguide size, and the speed of sound. The inequalities describing the upper-frequency limit and lower-frequency limit for an NIT with a square cross-section can be seen in Equations 17 and 18, respectively [76].

$$f_u < \frac{c}{2w} \qquad f_l > 0.01\frac{c}{s} \tag{17,18}$$

Also, the NIT testing must be conducted for at least some minimum time based on the microphone position, microphone spacing, and speed of sound to avoid inaccuracies from signal aliasing. However, most tests run significantly longer than this minimum; hence, it is not an issue. The minimum time value can be calculated using Equation 19 [76].

$$t \gg \frac{2(x_2 + s)}{c} \tag{19}$$

3.4.2 Grazing Flow Impedance Tube

A grazing flow running across the facesheet of an acoustic liner is known to have a strong non-linear effect on many areas of its performance [9], [73], [78]. As previously mentioned, non-linear effects can also arise when liners are exposed to high SPLs. While a two-microphone NIT testing method can characterize the non-linear effects of a sample under high SPLs, the effects of a grazing flow cannot be studied. Since aircraft acoustic liners are exposed to grazing flows during flight, the performance of liners under a grazing flow and high SPLs is very important. To test the effect of grazing flows on an acoustic liner in addition to high SPLs if desired, grazing flow impedance tubes (GFIT) are the preferred testing method [73]. A GFIT is similar to a typical wind tunnel except that somewhere near the middle of the wind tunnel is a section where an acoustic liner can be mounted. Also, near the liner sample, many microphone arrays are positioned around the sample, providing some of the data necessary to calculate the QOIs. Several compression drivers that inject sound waves into the flow are present upstream and downstream from the liner sample. Depending on which set of compression drivers are engaged defines whether an inlet or exhaust mode is present [73]. A picture of the GFIT at the NASA Langley Research Center is shown in Figure 18.

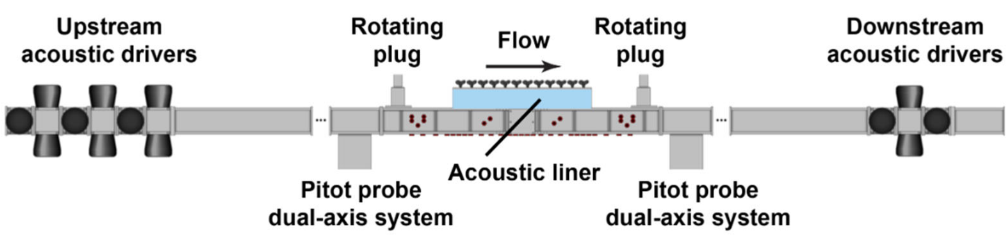

Figure 18. Diagram showing the GFIT at the NASA Langley Research Center (taken from [73]).

Calculating the QOIs from a GFIT test is significantly more complicated than a standard NIT. Therefore, only a brief qualitative description is given here; detailed equations can be found in [73]. Like the NIT, though, the calculation process is deemed an “impedance eduction” approach because it is based on pressure measurements, and impedance is not directly measured. One of the most common approaches to finding the impedance of a GFIT liner sample is to perform an inverse optimization such that the experimentally measured pressure field matches up with the pressure field from a computational aeroacoustic simulation [73], [78]. The sample acoustic impedance is a boundary condition that is varied in the simulation until a close match to the experimental data is found. It is important to note that other approaches can also be used to find the QOIs from a GFIT test, and developing methods to do so remains an active area of research. Also, an acoustic liner's aerodynamic drag can be determined using a GFIT [73].

3.4.3 Structural Testing

While there is a structural aspect to aircraft acoustic liners, it is a secondary concern relative to the acoustic, aeroacoustic, and aerodynamic performance. Nevertheless, it should be tested to verify that the basic load-bearing requirements are being met. The largest load most acoustic liners experience, outside a rare impact event during flight, is a technician standing on them during engine maintenance [8]. A simple quasistatic proof loading compression test using a hydraulic load frame can be used to test this scenario. A conservative approximate loading value would be double the weight of an adult male twenty years of age or older in the ninety-fifth weight percentile. Using data from the United States between 2015 and 2018, this loading value would be approximately equal to five hundred pound-force or twenty-two hundred newtons [79]. If the liner design can withstand this loading without facesheet cracking or plastic material deformation occurring anywhere, it should meet this requirement.

3.5 Acoustic Modeling and Simulation

Like the other branch, the acoustic modeling and simulation step can begin once the exported design files from the first step are received (assuming this branch is not being skipped). A model can be defined as a method or approach to describing some system of interest. A simulation uses a model to study the characteristics of some specific system. Three different acoustic modeling and simulation techniques can be employed, each providing a different fidelity level [9]. The modeling and simulation approaches used during workflow iterations depend on many factors like design maturity, available computational power, and overall iteration objectives.

3.5.1 Reduced Order Modeling

The low-fidelity approach uses reduced-order models (ROMs). A ROM, sometimes referred to as a surrogate model or metamodel, acts as a rapid transfer function between input variables and one or more QOIs. ROMs can be created by different methods ranging from physics-based analytical and semi-analytical equations (like Equation 3) to stochastic models like multiple linear regression, Gaussian process regression, and neural networks [80], [81]. ROMs can be the fastest evaluation method but are limited by what equations can be derived or the data available to train stochastic models. ROMs could be helpful early in the design process to do things like figure out suitable initial dimensions. Also, they could be helpful later in the development process when enough data is available to determine stochastic or semi-empirical models that emulate complex and computationally expensive simulations during an optimization loop. Many different scripting languages or data science software programs can be leveraged to implement ROMs.

3.5.2 Finite Element Method

The mid-fidelity approach is to run either transient or harmonic finite element method (FEM) simulations on coarsely meshed (about fifty to one hundred times fewer elements than the high-fidelity meshes) representations of the designs in an NIT. A few options for partial differential equations (PDEs) can be used to analyze liner designs. The most straightforward approach would be to use the Helmholtz equation, which can be seen in Equation 20 [82].

$$\frac{\omega^2}{K(\omega)} p_a + \nabla \cdot \frac{1}{\rho(\omega)} \nabla p_a = 0 \tag{20}$$

Since the Helmholtz equation is lossless, no sound attenuation can occur unless some sort of frequency-dependent homogenized material properties, damping, or acoustic impedance boundary conditions are applied. Also, the effects of different SPLs must be factored into these frequency-dependent properties to be able to consider that effect. Therefore, accurately determining these boundary conditions while not sacrificing a high degree of geometric fidelity can be challenging. However, if some adjustments, such as the facesheet can be approximated by a planar acoustic impedance boundary condition and viscous losses outside the facesheet region are negligible, then good results can be achieved. Typically, these simulations' geometry setup and QOI calculation process is the same as the two-microphone NIT testing method discussed previously.

If the facesheet simplification and no viscous losses assumptions are not acceptable, though, another approach that could be used is to conduct transient thermoviscous acoustic simulations. This approach can model the thermal and viscous sound attenuation that happens in small spaces meaning frequency-dependent properties are not needed. The linearized balance of mass and momentum equations for a viscous compressible and incompressible fluid, seen in Equations 21 and 22, are solved to do this [83].

$$\frac{1}{c^2}\frac{\partial P}{\partial t} + \nabla \cdot (\rho \vec{v}) = 0 \tag{21}$$

$$\rho \frac{\partial \vec{v}}{\partial t} - \nabla \cdot \sigma = 0 \tag{22}$$

In practice, the geometry setup and excitation source (except now a transient signal) used for the thermoviscous approach are essentially the same as the pressure acoustics method. In addition, no-slip boundary conditions must be applied to all the surfaces. Also, since a transient approach is used instead of a harmonic one, the QOI calculation process is different. Instead of two probes measuring acoustic pressure, a series of equally spaced probes throughout the waveguide measuring both acoustic pressure and acoustic particle velocity for each time step are used, as depicted in Figure 19. Using Equation 23 with the Fourier transformed probe values can be used to get the reflection and consequently the other QOIs that use the reflection as an input [9], [78].

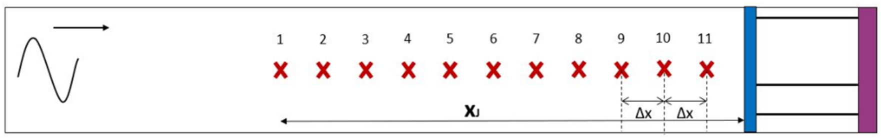

Figure 19. Example of geometry and probe setup used to calculate QOIs for a transient simulation (taken from [78]).

$$R = \frac{1}{N_{mics}} \sum_{i=1}^{N_{mics}} \frac{p_{a,i} - \rho c v_{a,i}}{p_{a,i} + \rho c v_{a,i}} \, e^{-2jkx_i} \tag{23}$$

Even with smaller meshes, the transient thermoviscous acoustics simulations can be very computationally expensive and time-consuming. One technique that can be used to reduce the computational expense is to solve the coupled harmonic pressure acoustics-thermoviscous acoustics problem instead, such that the computationally expensive thermoviscous losses are only evaluated in small regions and near walls where needed. Again, this coupled approach changes how the QOI calculation process works. For the new QOI calculation process, a line is "drawn" down the center of the tube to the start of the facesheet. Along this line, the complex acoustic pressure is sampled thousands of times uniformly. Then for each frequency value, a curve fit with the form seen in Equation 24 for the acoustic pressure as a function of waveguide position is performed using the Levenberg–Marquardt algorithm to minimize the residual sum of squares [84]–[86].

$$p_a(x_l) = (\beta_0 + j\beta_1)\, e^{x_l(-j\beta_2 - \beta_3)} + (\beta_4 + j\beta_5)\, e^{x_l(j\beta_2 + \beta_3)} \tag{24}$$

Then using the parameter values obtained during the curve fit, the reflection at the facesheet can be calculated using Equation 25 [86]. Optionally, a small correction factor is also applied to help fix low absorption coefficient predictions that can occur far away from resonant peaks. This calculation approach also works for the single-field thermoviscous approach when solving in the frequency domain.

$$R = \varepsilon\left(\frac{\beta_2 + j\beta_3}{\beta_0 + j\beta_1}\right)e^{2[\, j\beta_4 \cdot max(x_l) + \beta_5 \cdot max(x_l)\,]} \tag{25}$$

In recent years a few multiphysics software tools able to, directly and indirectly, couple many different fields together have become available. For example, a thermal-acoustic-thermoviscous acoustic-mechanical coupling could better simulate and evaluate acoustic liner behavior under the combined environments they would see in real life. Also, to characterize the effects of a liner under a grazing flow, computational fluid dynamics simulations can be used to determine a background flow which is then applied in pure acoustic simulations to characterize the flow's effect.

3.5.3 Lattice Boltzmann Method

The high-fidelity approach is to run transient acoustic simulations using the Lattice Boltzmann method (LBM) to evaluate a very finely meshed representation of liner geometry inside a NIT (using tens of millions of elements). The LBM is a computational fluid dynamics (CFD) method based on Ludwig Boltzmann's kinetic theory of gases [78]. At a basic level, the LBM method models the fluid as discrete particles that collide with other particles and advect as a function of time [78]. This contrasts the more commonly used CFD approaches based more on macroscopic properties. One advantage of the LBM approach is that it is not dissipative, which means that it correctly preserves acoustic perturbations, unlike the conventional Navier-Stokes CFD approach. By running acoustic LBM using the very large eddy simulation approach with similar setups to the FEM models discussed previously (geometric only) and no-slip boundary conditions, it is possible to highly resolve viscous losses and get accurate results. The acoustic performance QOI calculation approach is the same as the transient thermoviscous acoustics approach that used Equation 23.

3.6 Database & Optimization

The design, modeling/simulation, manufacturing, quality inspection, and empirical testing performed throughout a workflow produces a significant amount of data that is committed to a central database at the end of each iteration. As multiple iterations are conducted for one or more design configurations, an ensemble of data is created. An ensemble is a set of related runs that describe the same problem space, but the overall environment varies. As mentioned before, the desired optimization effect can be achieved by feeding all of this data back into previous steps such as manufacturing, design, and modeling/simulation.

To begin Chapter 3, a new iterative direct AM-focused design and development method consisting of five steps for aircraft acoustic liners is presented. The five workflow steps include: (1) design concept generation and solid modeling, (2) computational modeling and simulation, (3) prototype manufacturing and quality inspection, (4) physical testing of the prototypes, and (5) optimization and database development. The primary difference between the new approach and previous methods is the addition of the first and third steps, which could be essential for successfully developing the next generation of liners. Next, after introducing the new workflow, the components that make up each step were explained in detail. To test and demonstrate this new design and development method, a single iteration of the workflow is shown in Chapter 4.

Chapter 4

Design and Development Methodology Demonstration

The first iteration of an initial AM acoustic liner study utilizing multiple designs is presented in this chapter to demonstrate the design and development methodology from Chapter 3. Ultimately, the goal is to exhibit the effectiveness of this new approach. In this example, all five workflow steps are carried out. However, since multiple options are available within each of the primary steps, only a small subset of them was utilized. Similarly, in practice, only a subset of all the options and methods available within each primary step that further the desired goals would likely be implemented. Details on the primary and secondary steps for this specific example are shown in the following sections.

4.1 AM Acoustic Liner Design Concepts

As previously mentioned, the AM-focused workflow's first step is concept generation and 3D solid modeling. So to start, a single hollow consolidated liner assembly with a backplate, outside core walls, and facesheet was modeled in Ansys SpaceClaim 2022 R1[7] to act as a general template that could accommodate many different core design concepts. The generalized design template approach is an acceptable starting place for this initial study, but it does not take advantage of the individual customization allowed by AM. The sizing of the various liner features was mainly based on the required sample dimensions for the PSU NIT, the minimum feature sizes most standard desktop MEX printers could consistently make, and what would likely fit inside a thinner turbofan engine nacelle. The exact dimensions used can be seen in Appendix B. The most significant compromise with this set of dimensions was that the facesheet

[7] https://www.ansys.com/products/3d-design/ansys-spaceclaim

hole diameter had to be larger than the one-millimeter maximum used for most MPPs. However, this also allowed for some expected shrinkage in the nominal diameter to be accounted for. MEX was used in this case instead of the preferred MJT and VPP processes due to cost and availability constraints.

In total, the eight different SDOF liner design concepts that are pictured in Figure 20 were generated. To create all the 3D solid models needed for future workflow steps, nTopology nTop version 3.21 was used to generate and combine the core sections with the general liner template. Next, all designs were converted to a mesh-based geometry (MBG) from the implicit representation and exported as 3D manufacturing format (.3mf) files. Seven of the designs leveraged one of the AM liners/acoustic absorber concepts discussed during the literature review. Since much initial interest has revolved around surface-based lattices, five different TPMS surface-based homogeneous lattices, including a gyroid, Schwarz D, Schwarz P, lidinoid, and split P, were created. The other two AM design concepts used a stochastic strut-based Voronoi lattice and a conical spiral labyrinth, as shown in the figure. Also, a honeycomb core liner was printed to act as a baseline with which the new designs could be compared. All the core design specifications can be found in Appendix B within the same section as the general liner template dimensions.

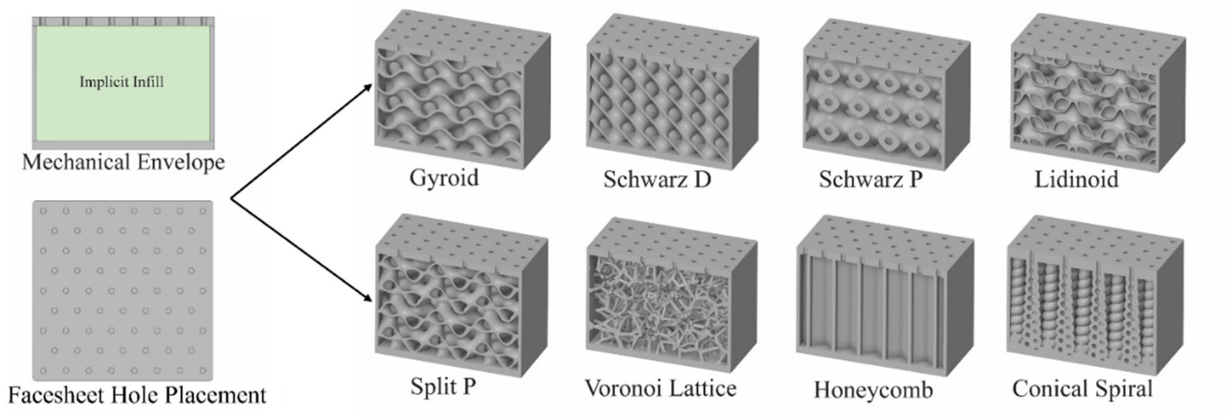

Figure 20. The general liner template and the eight different acoustic liner design concepts.

4.2 Prototype Manufacturing

For this study, both branches that become available after the 3D solid modeling phase were utilized. The branch containing sample manufacturing and quality inspection, followed sequentially by physical hardware testing, was completed first. Since MEX had already been designated as the AM process type to make these samples, the next step was to select one, or more, compatible materials to fabricate them. Two different materials were selected: (1) silver-colored 1.75 mm diameter polylactic acid (PLA) from Amazon Basics and (2) grey-colored 1.75 mm diameter thermoplastic polyurethane (TPU) from MatterHackers. These two specific materials were chosen because they were readily available and significantly differed in their elastic modulus. Specifically, TPU typically has a much lower stiffness under loading than PLA for the same shape. The goal was to see how much of an effect, if any, the acoustic loading force would have on the acoustic performance between the two.

After selecting the AM process type and two different materials, process planning was performed. To begin, each sample was imported into Ultimaker Cura version 4.13.1 and checked to ensure no facet defects or poor geometry approximations were present. Next, the orientation and position were selected, which was straightforward for all these designs because they were self-supporting and had flat backplates that could lay perfectly tangent to the build plate. Printing on the backplate was chosen over the side core walls to prevent stair-stepping on facesheet holes. In addition, only one design would be printed at a time in the middle of the build plate to prevent stringing between parts. The only non-default print feature added was a brim around the edges of the backplate to minimize warpage from thermal gradient-induced residual stresses. Finally, all components were sliced using the default process settings for both material types using a full internal infill and a 0.1 mm layer height on an Anycubic Vyper MEX desktop 3D printer. Before exporting the jobs to the printer, a layerwise visualization was leveraged to check that everything appeared to be working correctly. An example of the layerwise visualization for the PLA gyroid liner design can be seen in Figure 21.

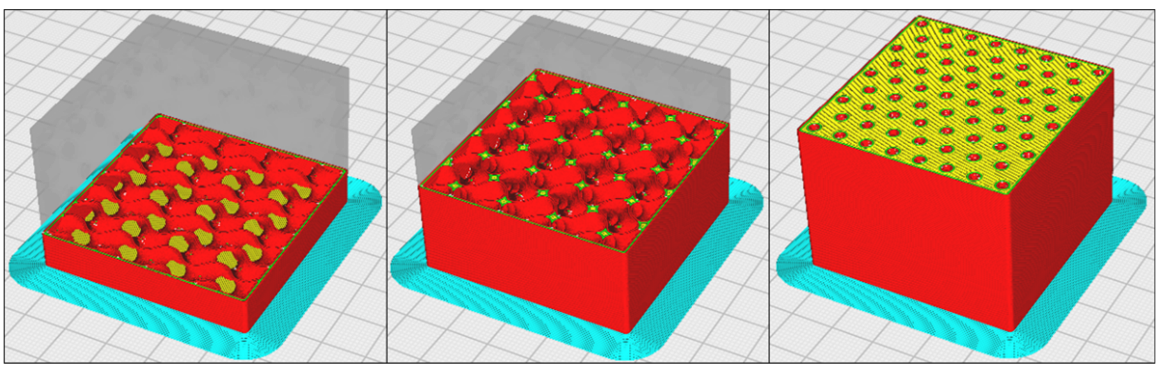

Figure 21. Layerwise build visualization for the PLA gyroid liner design.

Sixteen samples were printed, each of the eight designs in two different materials. The only post-processing required for this sample batch was to remove the brim (shown in blue in Figure 21) and clean up the edge where it was in contact with the liner samples using a deburring tool. All sixteen final liner prototype samples can be seen in Figure 22.

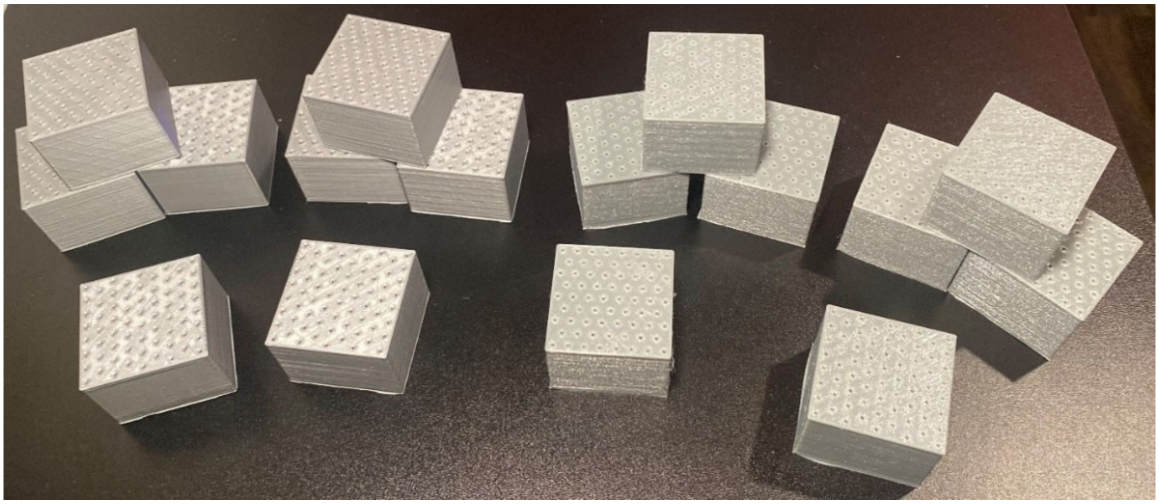

Figure 22. Picture of all sixteen printed liner samples, consisting of eight different designs, each made from PLA and TPU.

4.3 Sample Inspection

Since this study is meant to be an example, only basic quality inspection techniques that could be carried out for the sixteen different samples in a cost-effective and efficient manner were utilized. The leading inspection techniques that fit this criterion are (1) facesheet image analysis and (2) leak testing. However, since the MEX process allowed for the liner samples to be printed as a single part, testing for any acoustic leakage is unnecessary. Therefore, only facesheet image analysis was performed to inspect these samples, especially considering the uncertainty of MEX consistently making small facesheet holes.

An Nvidia Jetson Nano[8] single-board computer with a Raspberry Pi camera module v2[9] was used to capture images of each facesheet. With the open-source image analysis software ImageJ[10] version 153k, the facesheet pictures were captured directly from the camera so that an automated macro could analyze the facesheet hole shape metrics using the built-in particle

[8] https://developer.nvidia.com/embedded/jetson-nano-developer-kit
[9] https://www.raspberrypi.com/products/camera-module-v2/
[10] https://imagej.nih.gov/ij/

analysis module [87]. This setup allowed for all the samples to be scanned and analyzed quickly. An example of how the original photo was prepared for particle analysis by the macro for the PLA Schwarz P sample can be seen in Figure 23.

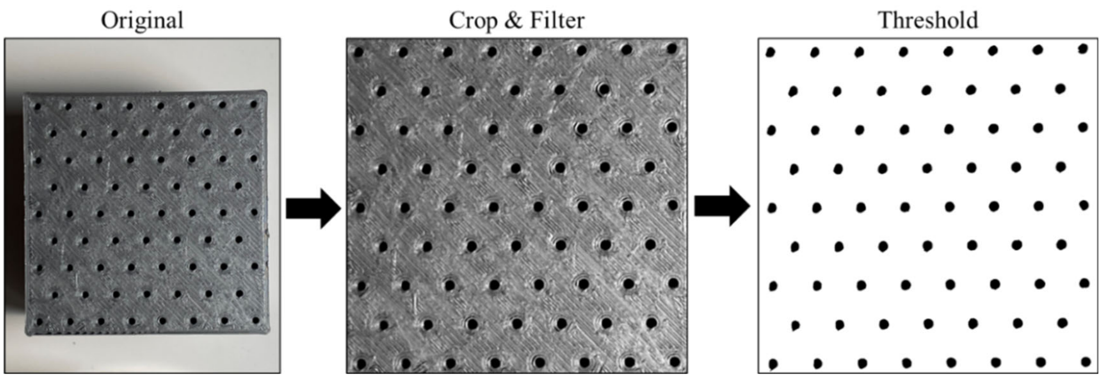

Figure 23. Example of facesheet hole image analysis picture processing steps for the PLA Schwarz P liner sample.

The ImageJ macro was configured to measure, log, and output the facesheet hole area, perimeter, major and minor axis length from a concentric ellipse fit, angle of the ellipse fit major axis from the image x-axis, and circular hole shape descriptors (i.e., circularity, aspect ratio, roundness, and solidity) [74], [87]. As seen in Figure 24, a multivariate Hotelling T-squared and generalized variance control chart were used to visualize these nine highly correlated parameters for a given liner [88]. Since the nine parameters are described as a single statistic, the interpretability of individual variables is lost, but the chart does show which facesheet holes are significantly different from the rest. This information helps find lower-quality facesheet holes so that they can potentially be fixed. For example, in Figure 24, three facesheet holes were flagged (red dots outside control limits). Investigating the individual parameter p-values showed it was due to low circularity values and high aspect ratios for these three holes. Unfortunately, little could be done to fix them since they were oversized and irregularly shaped. If the issue was something like excess material blocking the holes, though, that excess material could be removed to fix the problem.

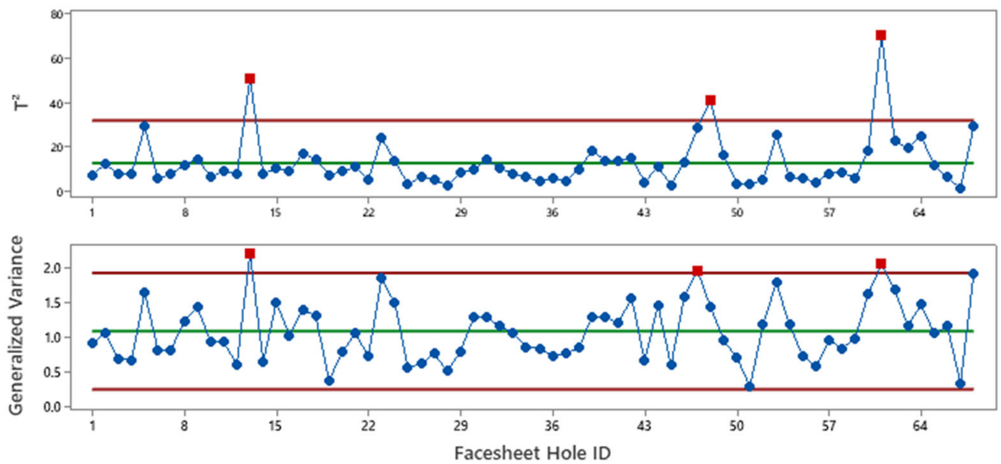

Figure 24. Multivariate Hotelling T squared and generalized variance control chart for the Schwarz P PLA facesheet hole image analysis.

While the Hotelling T-squared and generalized variance control charts provide information on process consistency and help detect poor-quality facesheet holes, they do not give any information on how well the printed facesheet hole dimensions match up with the nominal design. With the concentric ellipse fit data previously calculated, an approximation of the facesheet hole diameter deviation relative to the nominal value can be found with Equation 26.

$$d_{dev} \approx \sqrt{d_{major} * d_{minor}} - d \tag{26}$$

As an example, a histogram and kernel density estimation of the diameter deviation values for the same Schwarz P PLA liner is plotted in Figure 25 using Equation 26. As suspected, the plot showed that all facesheet holes experienced some shrinkage (negative deviation values). In the future, adjustments to the 3D solid model or process setting can be made to fix this.

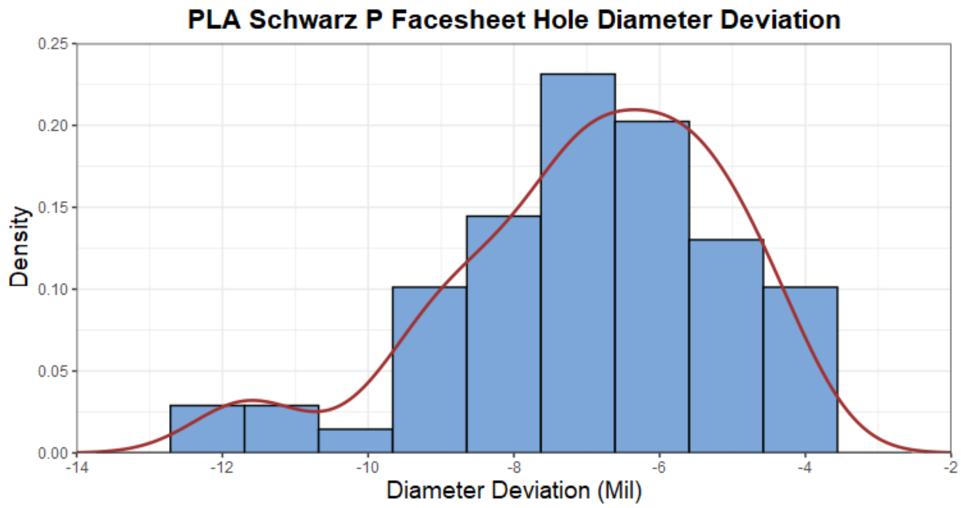

Figure 25. Histogram and kernel density estimation for the facesheet diameter deviation of the PLA Schwarz P liner sample.

4.4 NIT Testing

The two-microphone NIT testing rig at Penn State used to test these samples has a single 1.4 inch BMS 459ND-mid compression driver that is attached to a waveguide with a square cross-section of 2 inches x 2 inches. A Crown Audio Xti 2000 amplifier supplies power and controls the compression driver. The waveguide has a break in the middle so that samples can be easily inserted and removed. A plunger opposite the compression driver is used to adjust the position of the sample until the front surface sits flush with the interface between the waveguide sections. The distance from the compression driver to this interface is 33 cm. Also, the distance from the second microphone to the sample is 10 cm with a spacing of 3.75 cm between the microphones. The two microphones used for this NIT are both Brüel and Kjær 0.25 inch DeltaTron type 4944s. These microphones are connected to a compatible Brüel and Kjær DAQ. The DAQ data is processed and saved using the BK Connect software program. The NIT in this configuration has an approximate frequency range of 377 Hz to 3400 Hz with a maximum SPL of around 147 dB. A picture of the PSU NIT can be seen in Figure 26.

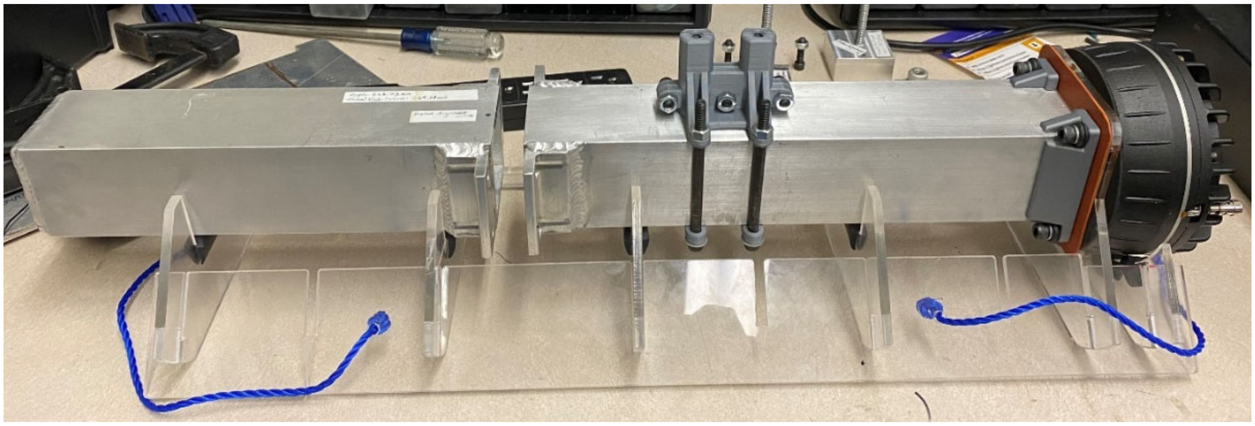

Figure 26. Picture of the Penn State NIT testing rig used to test all sixteen samples.

Before testing of the actual samples began, a few verification and validation tests were performed to check the NIT and Matlab post-processing scripts. It is important to note here that all microphones were calibrated beforehand. The most straightforward test was to push the plunger back some known distance and play a broadband noise at an SPL level of 130 dB for 30 seconds. Then by comparing the measured and theoretical cavity reactance values, it could be determined if the NIT and Matlab scripts are working correctly. The theoretical cavity reactance, in this case, is described by Equation 27 [9].

$$\chi = -j\cot\left(\frac{2\pi f}{c}D\right) = -j\cot\left(\frac{\omega}{c}D\right) = -j\cot(kD) \tag{27}$$

The experimental results of the test when the plunger was pushed back approximately 2.25 inches can be seen in Figure 27. As the plot shows, there was good agreement between the two curves.

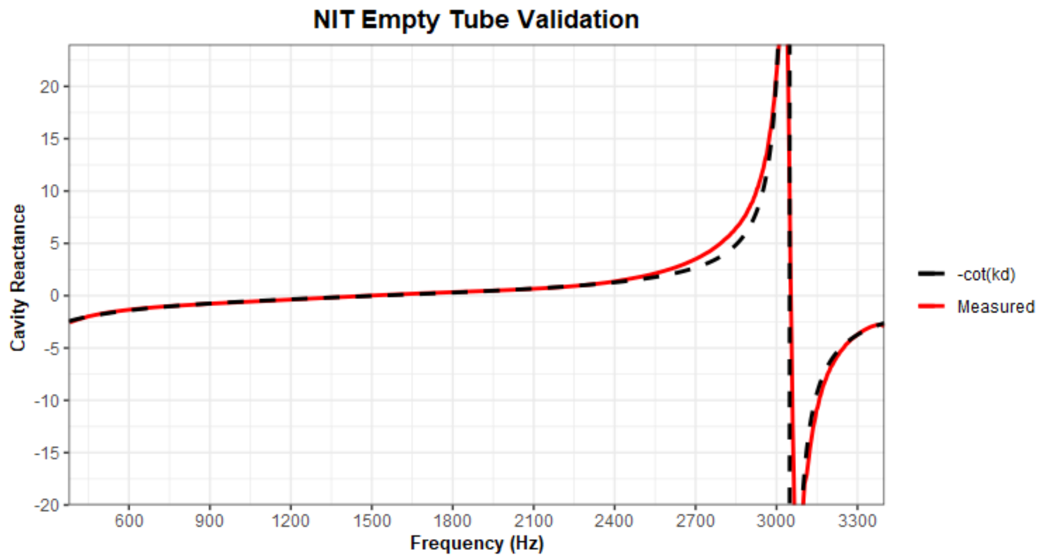

Figure 27. NIT validation plot comparing theoretical and measured empty cavity reactance.

Like the cavity reactance test, another similar experiment can be performed using a porous material with a known absorption curve instead of an empty volume. Sometimes this method is preferred over the empty cavity approach because an actual physical sample is being tested. Again, a broadband noise source was played for 30 sec at an SPL of 130 dB with a 1 inch thick American Acoustical Products Hushcloth sample. The Hushcloth sample and the comparison of the experimental results to the manufacturer data can be seen in Figure 28. Again, there was good agreement between the two curves being compared.

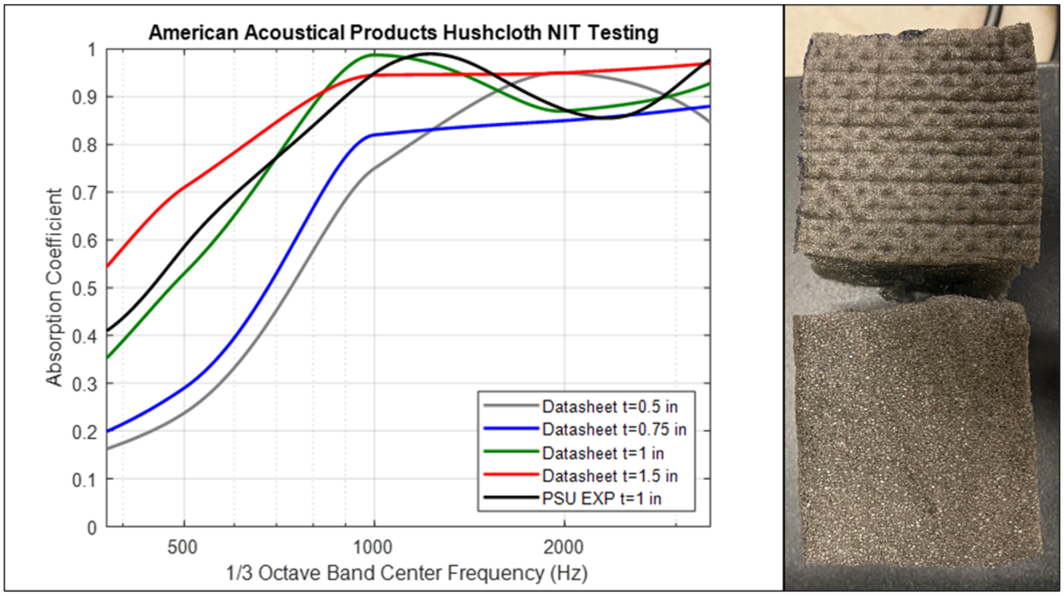

Figure 28. NIT validation plot comparing the measured and known absorption coefficient with a one-third octave band filter applied (green and black curves) for a one-inch thick hushcloth sample (pictured on the right).

Finally, a third test can be performed to ensure that the NIT can capture the non-linear effects of different SPL levels. To do this, a NASA AE01 specification benchmark sample with a honeycomb core was 3D printed with VPP and tested at four different SPL values to compare to published data [89]. When tested at 110 dB, 120 dB, and 130 dB, no large non-linear effect on attenuation was observed. However, when tested at the NIT's max SPL of 147 dB, a significant non-linear effect on attenuation was seen relative to the previous three tests. The comparisons of the four different SPL tests and a picture of the AE01 sample used can be seen in Figure 29.

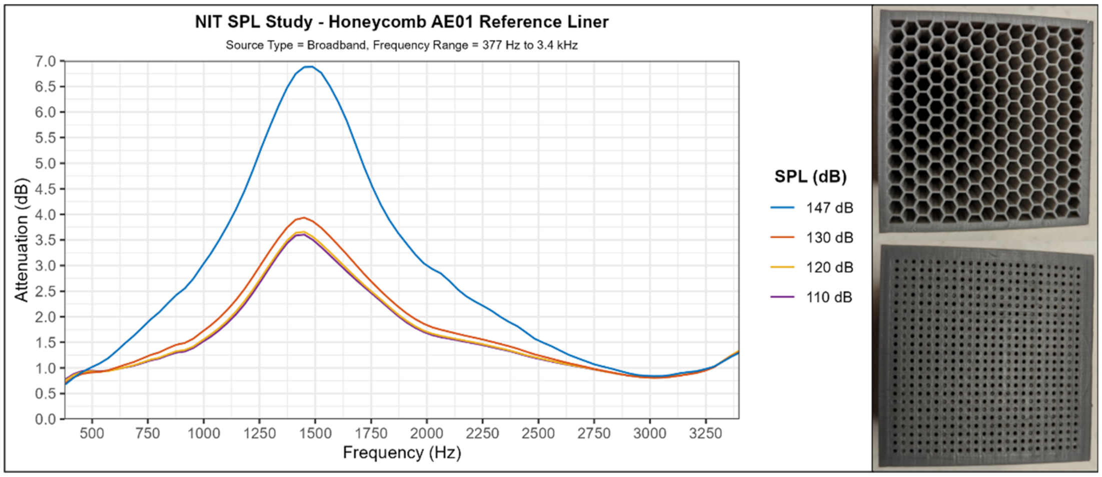

Figure 29. NIT validation plot using the NASA AE01 reference liner to check that non-linear effects at high SPL values can be measured. The sample used with no attached backplate is shown on the right.

After the NIT and Matlab scripts used for post-processing were validated and verified using these three tests, all sixteen 3D printed acoustic liner samples were tested. Each sample was tested three times at an SPL of 130 dB using a broadband noise source. The absorption coefficient results when all three runs for each design and material combination were averaged together can be seen in Figure 30.

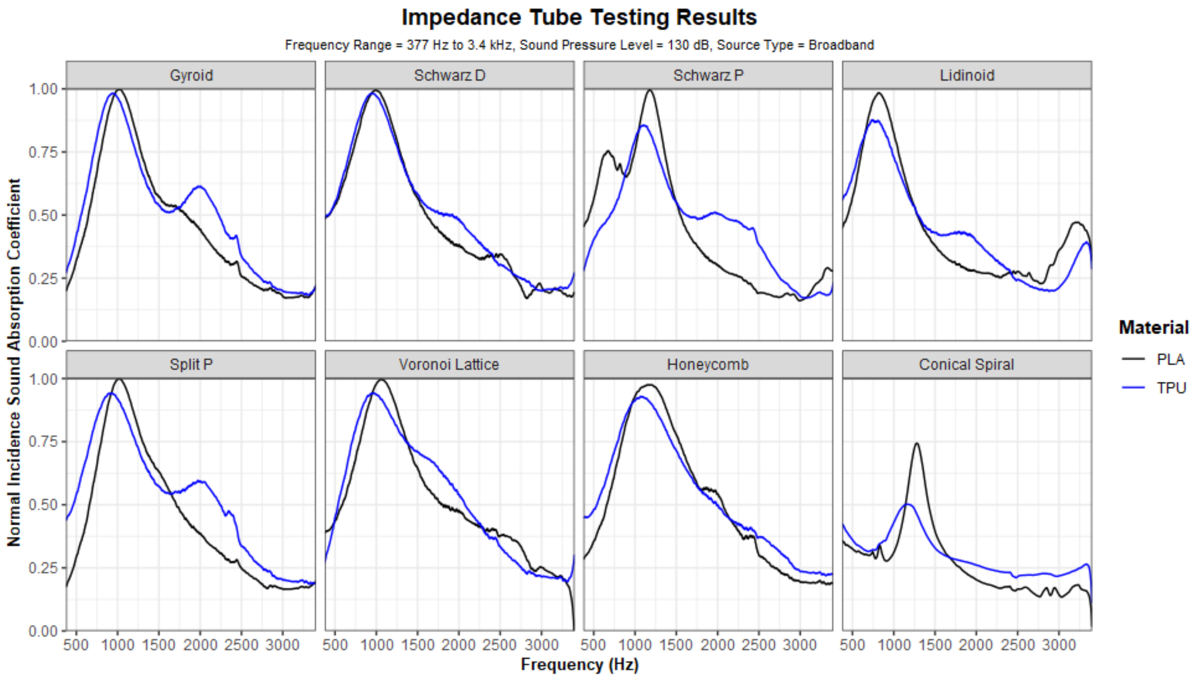

Figure 30. Plots showing the absorption coefficient for the different AM designs and materials.

All liner designs, except the conical spiral, showed good low to mid-frequency sound absorption, but absorption started to drop off towards the upper-frequency limit of the NIT. In particular, the designs that stood out were the Schwarz P and lidinoid because of some dual resonance behavior shown by both materials. Another observation for some designs is that there is a jump in the absorption coefficient difference for the different materials between about 1500 Hz and 2500 Hz. It is hypothesized that this results from the acoustic load causing significant facesheet vibrations for the semi-compliant TPU material used to fabricate those samples. Finally, the area under the absorption curve was numerically integrated, and a paired exact Wilcoxon signed-rank test was performed to test whether there was a statistically significant difference between the materials. The alternative hypothesis that the population median of the paired differences is less than zero (PLA minus TPU) was accepted with a p-value of 0.0078. The takeaway from this is that using semi-compliant AM materials can make a difference in performance and could be an interesting variable to manipulate and study when designing liners with different materials in the future.

4.5 Modeling and Simulation

After the branch containing the sample manufacturing, quality inspection, and physical testing activities was complete, the branch with the modeling and simulation activities began. The modeling and simulation in this study focused on designs that showed interesting behavior during NIT testing. In this case, the lidinoid and Schwarz P designs were selected due to some dual resonance absorption observed during testing. Therefore, to see how different mid-fidelity modeling and simulation techniques compare (to experimental data and each other), both designs were simulated using the harmonic pressure acoustics and coupled harmonic pressure acoustics-thermoviscous acoustics approach in openCFS[11] version 22.09 [90]. The mid-fidelity modeling and simulation techniques were used instead of the other two fidelity levels due to a lack of data, appropriate analytical models, and LBM solvers discussed in Chapter 3.

The harmonic pressure acoustics simulations were carried out first. As previously mentioned, one of the challenges with this method is determining the needed material properties or acoustic impedance boundary conditions while maintaining geometric fidelity and acceptable assumptions. A common way this is done when modeling simple empty cavity MPPs is to emulate the thermal and viscous facesheet losses using a frequency-dependent equivalent fluid or homogenized properties. For the simple case of empty cavity MPPs with circular facesheet holes, the facesheet is modeled as a solid block with no holes sitting on top of the empty cavity. This block's frequency-dependent complex density and compression modulus can be calculated using Zwikker and Kosten's model, shown in Equations 28 and 29 [91].

---

[11] https://opencfs.org

$$\tilde{\rho}_{eq}(\omega) = \frac{\rho}{\phi}\left[1 - \frac{2}{\sqrt{\frac{\omega\rho r^2}{\eta}}\sqrt{-j}} * \frac{J_1\left(\sqrt{\frac{\omega\rho r^2}{\eta}}\sqrt{-j}\right)}{J_0\left(\sqrt{\frac{\omega\rho r^2}{\eta}}\sqrt{-j}\right)}\right]^{-1} \tag{28}$$

$$\widetilde{K}_{eq}(\omega) = \frac{\gamma P_{atm}}{\phi}\left[1 + \frac{2(\gamma-1)}{\sqrt{\frac{\omega\rho r^2}{\eta}}\sqrt{-j * Pr}} * \frac{J_1\left(\sqrt{\frac{\omega\rho r^2}{\eta}}\sqrt{-j * Pr}\right)}{J_0\left(\sqrt{\frac{\omega\rho r^2}{\eta}}\sqrt{-j * Pr}\right)}\right]^{-1} \tag{29}$$

Alternatively, instead of defining the facesheet with the complex density and compression modulus, they could be used to calculate the normal surface impedance using Equation 30 [78]. If an impedance boundary condition is used to model the facesheet, then it would be a planar surface boundary condition. Equation 4, minus the cotangent cavity reactance term, would also be an acceptable way to find the facesheet acoustic impedance. The issue with these approaches is that they do not accurately model how sound propagates through facesheet orifices because they are just solid volumes and surfaces.

$$Z(\omega) = -j\sqrt{\widetilde{K}_{eq}(\omega)\tilde{\rho}_{eq}(\omega)} * \cot\left(\frac{\omega h}{c}\right) \tag{30}$$

A slightly adjusted approach was leveraged to address this issue with acoustic impedance and equivalent fluid geometric fidelity when simulating the Schwarz P and lidinoid liner samples. Instead of defining an equivalent fluid block for the whole facesheet, an equivalent fluid was defined inside each facesheet hole orifice volume. To find an accurate equivalent fluid, a calibration study was performed with Dakota[12] (Design Analysis Kit for Optimization and Terascale Applications) version 6.17 using the “nl2sol” trust-region non-linear least squares optimization method and the PLA honeycomb NIT testing data [85]. Doing this required making

[12] https://dakota.sandia.gov/

a CAD model of the fluid domain for the honeycomb sample inside the Penn State NIT. Then a quarter symmetry model of the fluid domain was meshed in nTop version 3.21 using four-node tetrahedral elements with position-dependent sizing such that they were more refined in and around the liner volume. The CAD model and quarter symmetry mesh is shown in Figure 31.

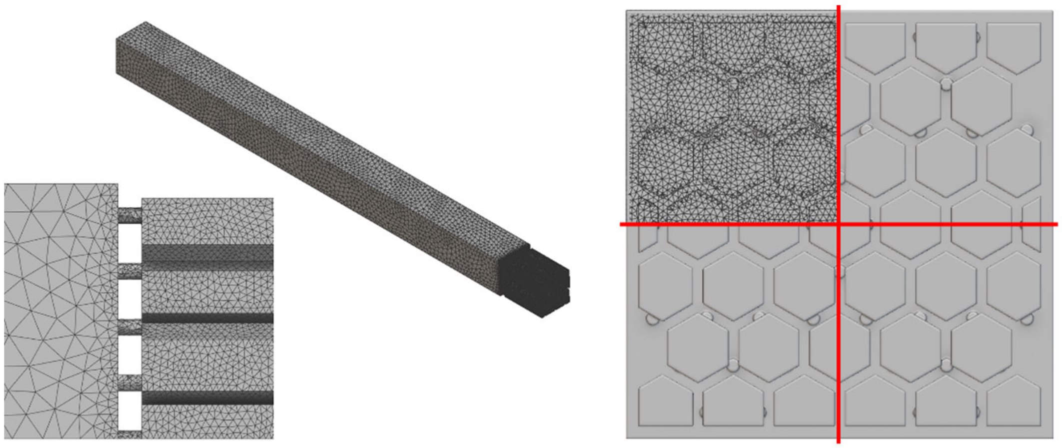

Figure 31. Picture of quarter-symmetry four-node tetrahedral mesh with position-dependent sizing for the honeycomb liner.

The regions beside the facesheet holes were defined as normal atmospheric air. The facesheet holes, on the other hand, had the real and imaginary terms of the complex density and complex compression modulus defined by parametrized two-term power law equations that are a function of frequency. Only two boundary conditions were applied: (1) a pressure excitation source on the face opposite the sample and (2) sound hard rigid walls on all surfaces. In this case, the sound hard walls (i.e., homogeneous Neumann boundary condition [82]) account for symmetry. However, if antisymmetry is present, then a sound soft wall (i.e., homogeneous Dirichlet boundary condition [82]) should be applied to the symmetry surfaces. Finally, Dakota performed a series of automated asynchronous parallel evaluations to find terms for the parameterized equivalent fluid equations that minimized the residuals between the experimental and simulated absorption coefficients over the NITs frequency range. Only the PLA data was used for calibration since the TPU facesheet vibrations would be challenging to model. Equations 31 and 32 show the calibrated equations for the facesheet hole complex density and complex compression modulus that were determined with the honeycomb model during the Dakota study.

$$\tilde{\rho}_{eq} = 0.1142860251 * (f)^{-10.60483781} + 1.933930036 + j\{0.001020341417 * (f)^{-41.08429251} + 1.233969492\} \tag{31}$$

$$\widetilde{K}_{eq} = 0.02220949433 * (f)^{1.770097217} + 7.539296893 + j\{-1.463816335E - 05 * (f)^{2.934529065} + 0.9925217259\} \tag{32}$$

The equivalent fluid determined during the Dakota study with the Honeycomb NIT data can now be applied to any other design with the same facesheet to simulate its behavior. It is important to note, however, that this approach assumes the viscous losses in the core section behind the facesheet are insignificant and that all the core does is redirect impinging sound waves. While this might be a reasonable assumption for some designs, it could lead to inaccuracies for others when the viscous losses in the core are significant. Nevertheless, it was determined that this would be an acceptable assumption for simulating the Schwarz P and lidinoid designs due to the large unit cell size and low volume fraction they use relative to the overall liner. Therefore, harmonic pressure acoustics simulations were performed on both the Schwarz P and lidinoid designs using this equivalent fluid.

The preprocessing approach used for both designs was similar to the Honeycomb. Initially, fluid domain CAD models of both samples inside the Penn State NIT were created. Like the honeycomb model, the Schwarz P design was able to leverage quarter-symmetry; however, the lidinoid design could only use half symmetry. Due to the complex meshes needed for simulating lattices, taking advantage of symmetry whenever possible to reduce computational expense is highly recommended. Next, both models were meshed in nTop version 3.21 using four-node tetrahedral elements with position-dependent sizing. Finally, the same boundary conditions and materials used for the honeycomb simulation were applied, and the problems were executed. The simulation results for the Schwarz P and lidinoid can be seen in Figure 32 and 33, respectively.

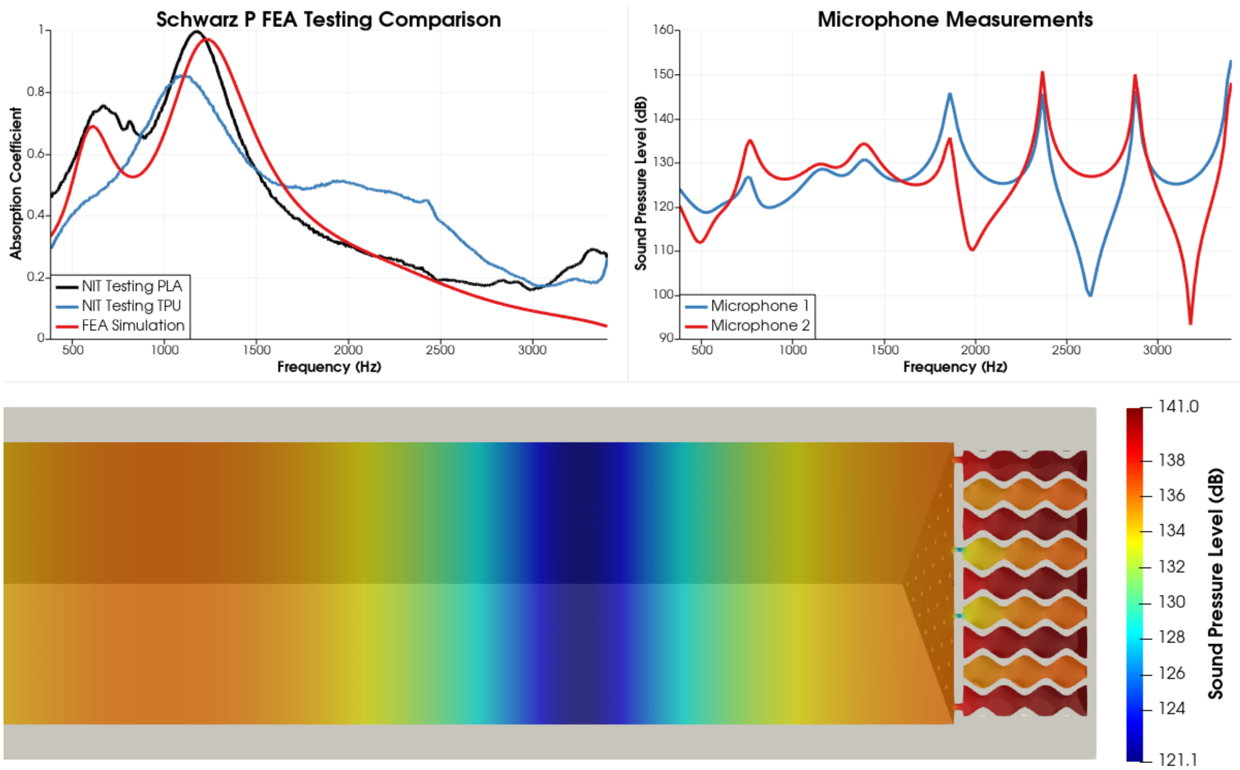

Figure 32. Schwarz P harmonic acoustic simulation results. The SPL field pictured is the response at a frequency value of 803.06 Hz.

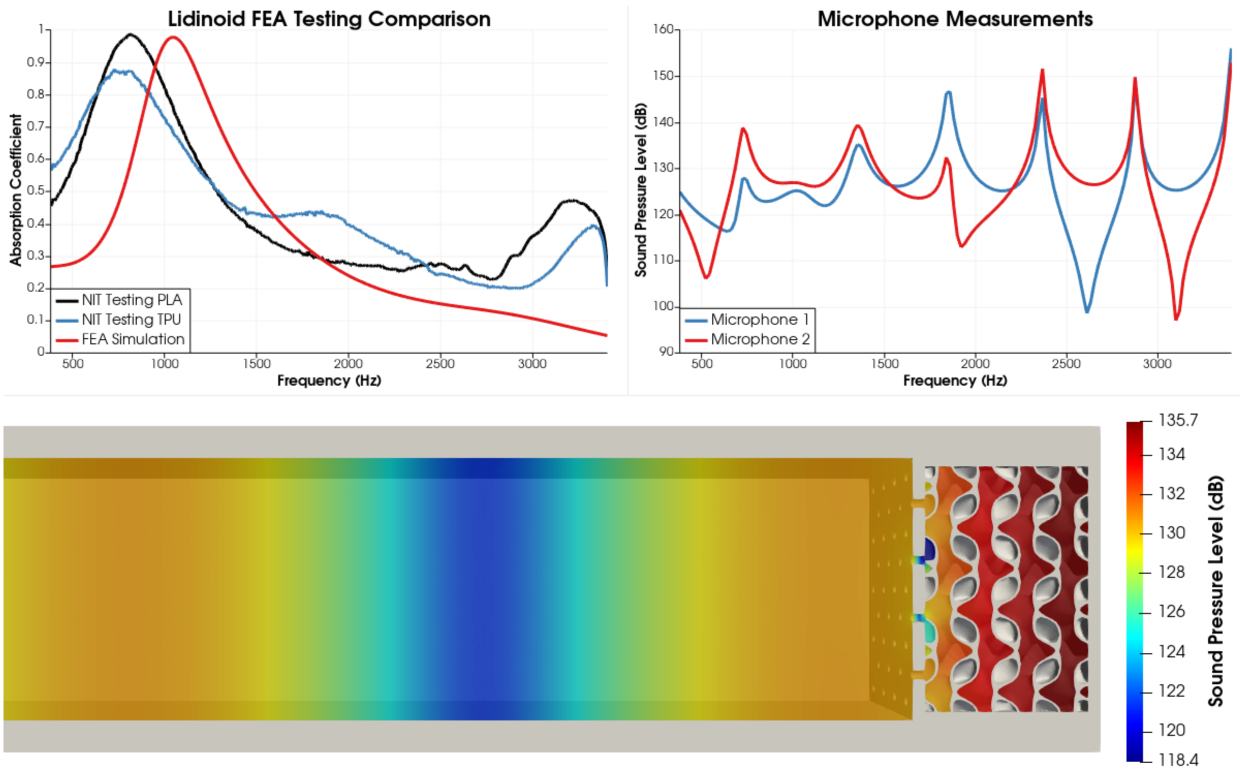

Figure 33. Lidinoid harmonic acoustic simulation results. The SPL field pictured is the response at a frequency value of 1249.41 Hz.

For the Schwarz P, the simulation predicted absorption coefficient matched the experimental NIT results well until it began to drop off around 2500 Hz. Comparing the experimental and predicted Schwarz P absorption coefficient data showed a mean absolute error (MAE) of about 0.08 with a root mean square error (RMSE) of about 0.1. The lidinoid simulation prediction, on the other hand, showed low absorption coefficient predictions near the lower and upper-frequency limits but did an okay job matching the experimental data between them. Comparing the experimental and predicted lidinoid absorption coefficient data showed an MAE of about 0.19 and an RMSE of about 0.23. Overall the predictions made with these simulations turned out to be reasonably close, showing that this equivalent fluid facesheet hole calibration approach using NIT data can be leveraged if the geometry meets the necessary assumptions.

In the absence of experimental data, another method to calibrate a facesheet hole equivalent fluid would be using the absorption coefficient found with Equations 3 and 4, along with a matching empty cavity liner model. Alternatively, if the effects of a grazing flow want to be studied, Equation 33 can be used instead of Equation 3 to get the target absorption coefficient values [8], [9]. One benefit these analytical models used in junction with a matching empty cavity liner have over the experimental approach is that they can be used over a broader frequency range (assuming the proper accompanying virtual NIT dimensions are used).

$$Z_{gf} = \frac{M}{\phi\left(2 + \frac{157\delta}{125d}\right)} + j\left\{\frac{\omega h}{\phi c}\left(\frac{1}{\sqrt{\frac{\omega \rho d^2}{2\eta} + 9}} + \frac{16d\left(\frac{7\sqrt{\phi}}{10} - 1\right)}{3\pi h(305M^3 + 1)} + 1\right) - \cot\left(\frac{\omega D}{c}\right)\right\} \quad (33)$$

After the harmonic pressure acoustic simulations for the Schwarz P and lidinoid designs were complete, each design was simulated again using the coupled harmonic pressure acoustics-thermoviscous acoustics technique. The goal with this simulation is to see how this approach compares to the equivalent fluid calibration method in addition to the experimental data. As previously mentioned, the most significant benefit of this method is that no frequency-dependent homogenized material properties, material damping, or acoustic impedance boundary conditions are required. This is because the thermal and viscous losses occurring when the sound propagates in small spaces and near walls are resolved. However, solving the thermoviscous problem over the entire domain is very computationally expensive, especially for complex designs like lattices. The computational expense can be reduced by coupling the pressure acoustics and thermoviscous acoustics because the thermal and viscous losses only have to be resolved where needed by walls and in small spaces. Also, the geometry can be adapted to evaluate different frequency ranges similar to before.

The same quarter-symmetry and half-symmetry meshes for the Schwarz P and lidinoid from the first simulation can be used again for the coupled problem; however, some of the boundary conditions and materials need to be adjusted. The two boundary conditions that remain the same as from the equivalent fluid problem are the pressure excitation source on the back surface across from the sample and the sound hard wall definition for all surfaces. For materials, instead of defining two different fluids like in the initial simulations, the entire domain is set as atmospheric air. Also, all the surfaces besides the ones used for symmetry and the excitation source are selected. For this selection of surfaces, a boundary layer where thermal and viscous losses need to be resolved is set. Finally, the problems can be run, and the QOIs are calculated at the facesheet using the inverse optimization approach with Equations 24 and 25. Results for both designs can be seen in Figure 34.

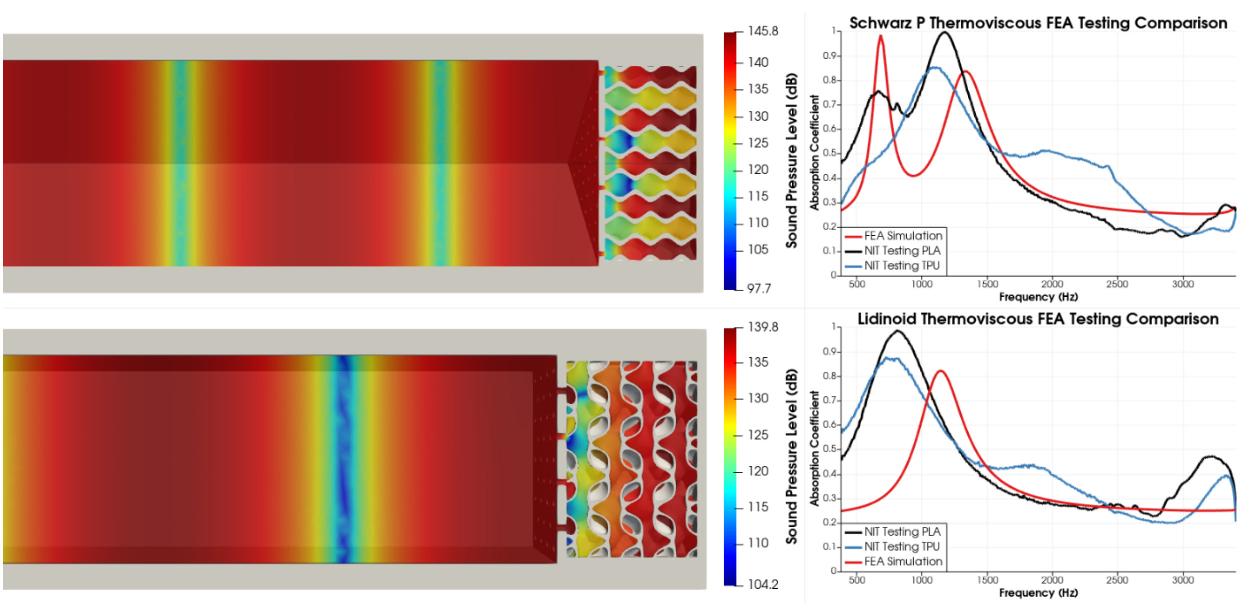

Figure 34. Schwarz P and lidinoid coupled harmonic pressure acoustics-thermoviscous acoustics simulation results. The SPL fields pictured are the responses at a frequency value of 1898.64 Hz.

The absorption coefficient predictions for the thermoviscous Schwarz P simulation showed good agreement with experimental data around the NIT's lower and upper-frequency limits. Also, the frequencies at which the two resonance peaks occur match well; however, the magnitude of the two absorption peaks and how the absorption changes between them were not well predicted. Comparing the experimental and predicted Schwarz P absorption coefficient data showed an MAE of about 0.11 and an RMSE of about 0.15. The lidinoid design's absorption coefficient prediction was pretty low in the first half of the frequency range. However, the absorption prediction started to match up better in the second half of the frequency range. Also, the resonance frequency was slightly higher than the experimental observation but not too far. Comparing the experimental and predicted lidinoid absorption coefficient data showed an MAE of about 0.15 and an RMSE of about 0.23. Overall, the equivalent fluid approach was more accurate (lower MAE and RMSE values), most likely because experimental data was used to calibrate the facesheet equivalent fluid allowing other factors like surface roughness to be indiscriminately taken into account.

The acoustic behavior of the Schwarz P and lidinoid liner designs was explored in depth using NIT testing, harmonic pressure acoustic simulations, and coupled harmonic pressure acoustics-thermoviscous acoustic simulations. However, how they would behave when exposed to a grazing flow is unknown. Therefore, to get an idea of their aeroacoustic performance at different grazing flow Mach numbers, the acoustic impedance values measured during NIT testing were plugged into a virtual GFIT similar to the NASA one previously discussed [92]. Again, the openCFS simulation code was used [90]. The boundary conditions used can be seen in Figure 35. Also, the results for the PLA Schwarz P design at 1932.22 Hz and a Mach number of 0.75 can be seen in Figure 36.

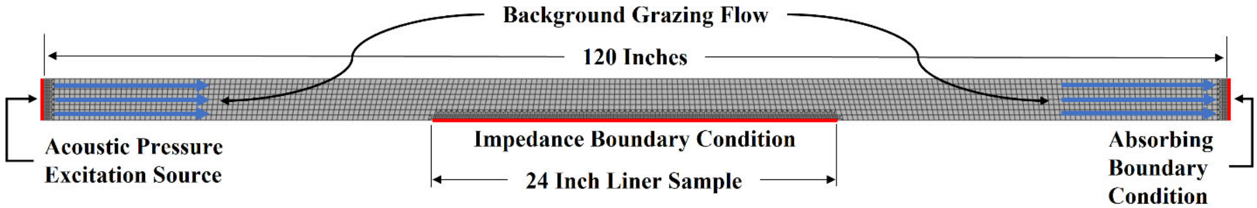

Figure 35. Geometry and boundary conditions for the GFIT simulations. The mesh consisted of 20-node hexahedral elements with local refinements on surfaces where boundary conditions are applied.

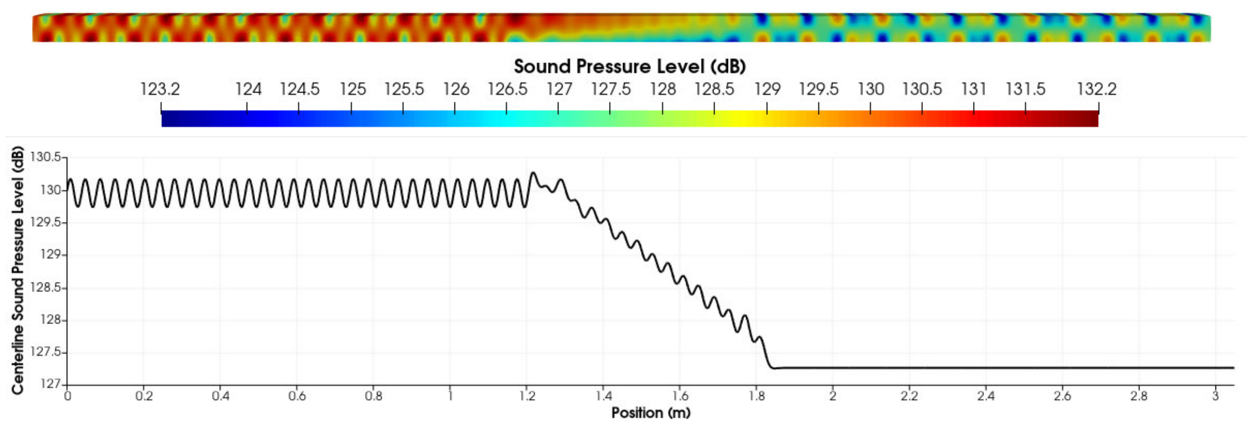

Figure 36. Schwarz P PLA GFIT simulation results. The SPL field pictured is the response at a frequency value of 1932.22 Hz with a grazing flow Mach number of 0.75.

To compare all the combinations of Mach number, material, and design, the plane wave transmission loss was determined using Equation 34 [3]. The plot comparing all the transmission losses can be seen in Figure 37. No clear trend between these different input variable combinations is easily observable, but the transmission loss was generally lower at higher Mach numbers.

$$TL = 10\log_{10}\left(\frac{W_i}{W_t}\right) \tag{34}$$

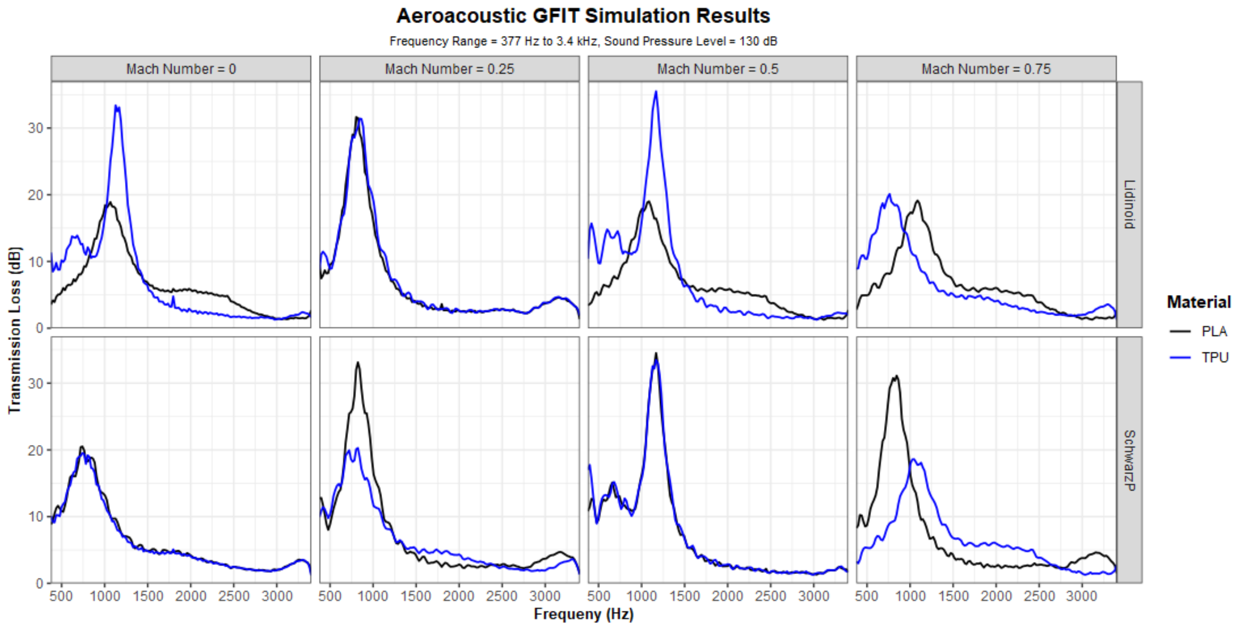

Figure 37. Plots showing the transmission loss for the different AM designs and materials under different grazing flows. The experimental NIT data was used instead of the finite element results.

4.6 Database Development, Data Analysis, and Optimization

To visualize all of the data collected during the 3D solid modeling phase, manufacturing, quality inspection, modeling and simulation, and physical testing, the scalable ensemble analysis and visualization tool SLYCAT[13] was leveraged. A picture of the SLYCAT interface can be seen in Figure 38. It has many functional modules for data analysis, including correlation analysis, clustering, time-series analysis, and anomaly detection, to name a few. Also, SLYCAT acts as a centralized web-based data storage place that is easy to access from any browser. If another iteration were to be performed, all of this data and analysis in SLYCAT could be leveraged to determine the next best steps.

[13] https://github.com/sandialabs/slycat

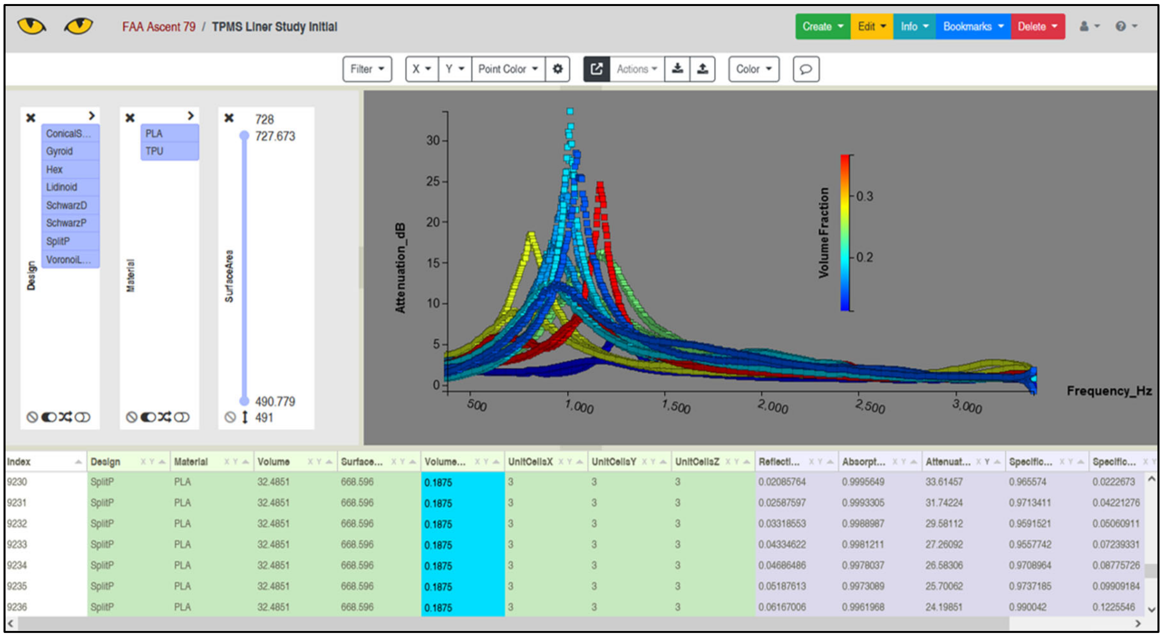

Figure 38. Analysis of all workflow data using SLYCAT.

This chapter presents the first iteration of an initial AM acoustic liner study utilizing multiple design configurations. The purpose of this study was to demonstrate the design and development methodology from Chapter 3. To begin, seven different SDOF AM liner designs leveraging concepts from the literature review and one baseline honeycomb sample were created in SpaceClaim and nTop. Next, the eight designs were each printed out of two materials (PLA and TPU) using an Anycubic Vyper MEX printer. Then, the quality of the newly fabricated samples is quantified using image analysis on the facesheets. After the manufacturing and quality inspection, all samples were tested using the Penn State NIT. Once testing is complete, several harmonic acoustic and aeroacoustic finite element simulations were run, and the results were compared to the NIT testing. Finally, all of the results and data from the proceeding steps are imported into a central database and analyzed in SLYCAT. Overall the new design and development method appeared to be successful; a plethora of good data was collected, which provides a path forward for another future iteration that improves upon the previous one.

Chapter 5

Conclusions and Future Work

The main objective of this research was to propose and test a new workflow that would support the design and development of novel AM acoustic liners that could meet the noise reduction, size, and weight requirements of future turbofan engines. To propose an effective AM-focused workflow, an initial literature review was conducted looking at acoustic liner background theory, conventional acoustic liner research, early research on AM liners/absorbers, and the current development process for conventional liners. Based on the learnings and gaps identified during the literature review, a new five-step development methodology for AM acoustic liners was proposed with the following steps:

1. Design concept generation and solid modeling
2. Prototype manufacturing and quality inspection
3. Computational modeling and simulation
4. Physical testing of the prototypes
5. Optimization and database development

Following the introduction of the AM acoustic liner workflow, the specifics of how the new design and development method works and details about each step's options were given. Then, one iteration of an initial design study was performed to demonstrate the workflow. Overall, the workflow was successful and provided a wealth of information that could be used to initiate another iteration that would build on the previous results. Despite the achievements of the new method, several weaknesses that could be improved upon in the future within each workflow step were identified.

The design concept generation and solid modeling step showed several strengths, such as flexibility with various design concepts regardless of geometric complexity and application of the latest solid modeling software tools. However, it was evident that transferring the final solid model to the proceeding workflow steps was time-consuming and labor-intensive. In particular, creating MBG representations from implicit models of the final design that had a good balance between file size and tesselation accuracy was challenging. Therefore, one potential future research project that could be conducted to address this issue would be developing a software toolchain that reliably automates this CAD data transfer process.

As expected during the prototype manufacturing and quality inspection step, both MEX and VPP processes were able to create complex acoustic liner geometries at the required feature resolution. However, some issues with post-processing and geometric accuracy were encountered. In particular, removing excess material and supports for parts made with VPP was not entirely possible unless the liner was printed in multiple pieces. Printing liner prototypes in multiple pieces is not ideal, and it avoids using one of AM's biggest strengths. Consequently, a future research project investigating different devices/processes able to remove excess material and supports from fully consolidated VPP liners would be highly beneficial. Also, both MEX and VPP had trouble making facesheet holes that accurately matched nominal design specifications. The main issues observed were rounded edges and hole shrinkage. Therefore, another potentially productive research project in the future would be performing a process parameter optimization study to minimize the difference between the nominal and as-printed geometries for the AM processes of interest.

Both the computational modeling/simulation and physical hardware testing provided adequate data quantifying the acoustic performance of various design concepts. However, as seen in Chapter 4, there was a decent amount of disagreement between the computational analysis and experimental measurements. Currently, the reasoning for these differences is not precisely known. However, factors like surface roughness, the difference in nominal versus as-printed geometry, and mechanical vibrations (to name a few) may be responsible. As a result, a potentially good research project in the future would be investigating methods to close the gap between simulation and empirical testing. This could be accomplished by doing things such as coupling additional fields to the acoustic analysis or developing new meshing methods that better represent the as-printed sample.

Finally, the optimization and database development demonstrated many strengths, such as providing a centralized location where all stakeholders can access information whenever needed and including additional data outside typical design and performance specs that could be valuable, such as manufacturing and quality details. Deciding what information should be included and keeping the database organized and up to date is a time-consuming task. Therefore, a research project that could be of substantial use here in streamlining this process would be creating software that automates documentation writing and database updates. In conclusion, the use of AM technologies for aircraft acoustic liner applications is an emerging field, so it will be interesting to see how it progresses in the future.

References

[1] "Novel Noise Linear Development Enabled by Advance Manufacturing – Ascent." https://ascent.aero/project/novel-noise-linear-development-enabled-by-advance-manufacturing/ (accessed Feb. 02, 2023).

[2] FAA Center of Excellence for Alternative Jet Fuels & Environment, "Ascent." https://ascent.aero/ (accessed Feb. 02, 2023).

[3] M. Crocker and J. Arenas, *Engineering Acoustics*. Hoboken: John Wiley & Sons Ltd, 2020.

[4] C. L. Nickol and W. J. Haller, "Assessment of the Performance Potential of Advanced Subsonic Transport Concepts for NASA's Environmentally Responsible Aviation Project," in *54th AIAA Aerospace Sciences Meeting*, San Diego, Jan. 2016. doi: 10.2514/6.2016-1030.

[5] D. L. Sutliff, D. M. Nark, and M. G. Jones, "Multi-degree-of-freedom liner development: Concept to flight test," *Int J Aeroacoust*, vol. 20, no. 5–7, pp. 792–825, Sep. 2021, doi: 10.1177/1475472X211023860.

[6] M. Gorji-Bandpy and M. Azimi, "Technologies for jet noise reduction in turbofan engines," *Aviation*, vol. 16, no. 1, pp. 25–32, Mar. 2012, doi: 10.3846/16487788.2012.679770.

[7] T. Elnady, "Modelling and Characterization of Perforates in Lined Ducts and Mufflers," The Royal Institute of Technology, Stockholm, 2004. Accessed: Mar. 03, 2023. [Online]. Available: http://kth.diva-portal.org/smash/get/diva2:9676/FULLTEXT01.pdf

[8] M. G. Jones, F. Simon, and R. Roncen, "Broadband and Low-Frequency Acoustic LinerInvestigations at NASA and ONERA," *AIAA Journal*, vol. 60, no. 4, pp. 2481–2500, 2022, doi: 10.2514/1.J060862.

[9] J. Winkler, J. M. Mendoza, C. A. Reimann, K. Homma, and J. S. Alonso, "High fidelity modeling tools for engine liner design and screening of advanced concepts," *Int J Aeroacoust*, vol. 20, no. 5–7, pp. 530–560, Sep. 2021, doi: 10.1177/1475472X211023884.

[10] "Additive manufacturing — General principles —Fundamentals and vocabulary," *ISO/ASTM 52900:2021(E)*. 2021.

[11] J. O. Milewski, *Additive Manufacturing of Metals From Fundamental Technology to Rocket Nozzles, Medical Implants, and Custom Jewelry*. Springer International Publishing, 2017. doi: 10.1007/978-3-319-58205-4.

[12] I. Gibson, D. Rosen, B. Stucker, and M. Khorasani, *Additive Manufacturing Technologies*. Springer, 2015.

[13] M. K. Thompson *et al.*, "Design for Additive Manufacturing: Trends, opportunities, considerations, and constraints," *CIRP Ann Manuf Technol*, vol. 65, no. 2, pp. 737–760, 2016, doi: 10.1016/J.CIRP.2016.05.004.

[14] J. Schmelzle, E. v Kline, C. J. Dickman, E. W. Reutzel, G. Jones, and T. W. Simpson, "(Re)Designing for Part Consolidation: Understanding the Challenges of Metal Additive Manufacturing," 2015, doi: 10.1115/1.4031156.

[15] S. Yang and Y. F. Zhao, "Additive manufacturing-enabled design theory and methodology: a critical review," *International Journal of Advanced Manufacturing Technology*, vol. 80, no. 1–4. Springer London, pp. 327–342, Sep. 19, 2015. doi: 10.1007/s00170-015-6994-5.

[16] Z. Doubrovski, J. C. Verlinden, and J. M. P. Geraedts, "Optimal Design for Additive Manufacturing: Opportunities and Challenges," in *ASME 2011 International Design Engineering Technical Conferences and Computers and Information in Engineering Conference* , Washington, DC: The American Society of Mechanical Engineers, Jun. 2012. doi: https://doi.org/10.1115/DETC2011-48131.

[17] F. Laverne, F. Segonds, N. Anwer, and M. le Coq, "Assembly based methods to support product innovation in design for additive manufacturing: An exploratory case study," *Journal of Mechanical Design, Transactions of the ASME*, vol. 137, no. 12, Dec. 2015, doi: 10.1115/1.4031589.

[18] C. J. Tuck, R. J. M. Hague, M. Ruffo, M. Ransley, and P. Adams, "Rapid manufacturing facilitated customization," *Int J Comput Integr Manuf*, vol. 21, no. 3, pp. 245–258, Apr. 2008, doi: 10.1080/09511920701216238.

[19] A. Garland and G. Fadel, "Design and Manufacturing Functionally Gradient Material Objects with an off the Shelf Three-Dimensional Printer: Challenges and Solutions," *Journal of Mechanical Design, Transactions of the ASME*, vol. 137, no. 11, Nov. 2015, doi: 10.1115/1.4031097.

[20] J. Arenas and M. Crocker, "Recent Trends in Porous Sound-Absorbing Materials," *Sound & Vibration*, vol. 44, no. 7, pp. 12–17, 2010.

[21] "Different absorber types within room acoustics." https://www.troldtekt.com/knowledge/good-acoustics/advanced-acoustics/different-absorber-types/ (accessed Jan. 21, 2023).

[22] D.-Y. Maa, "Potential of microperforated panel absorber," *J Acoust Soc Am*, vol. 104, no. 5, pp. 2861–2866, Nov. 1998, doi: 10.1121/1.423870.

[23] R. H. Bolt, "On the Design of Perforated Facings for Acoustic Materials," *J Acoust Soc Am*, vol. 19, no. 5, pp. 917–921, Sep. 1947, doi: 10.1121/1.1916641.

[24] C. Zwikker and C.W. Kosten, *Sound Absorbing Materials*. Elsevier Pub. Co., 1949.

[25] J. M. A. Smits and C. W. Kosten, "Sound absorption by slit resonators," *Acta Acustica united with Acustica*, vol. 1, no. 3, pp. 114–122, 1951.

[26] U. Ingard, "On the Theory and Design of Acoustic Resonators," *J Acoust Soc Am*, vol. 25, no. 6, pp. 1037–1061, Nov. 1953, doi: 10.1121/1.1907235.

[27] U. Ingård and R. H. Bolt, "Absorption Characteristics of Acoustic Material with Perforated Facings," *J Acoust Soc Am*, vol. 23, no. 5, pp. 533–540, Sep. 1951, doi: 10.1121/1.1906799.

[28] D. B. Callaway and L. G. Ramer, "The Use of Perforated Facings in Designing Low Frequency Resonant Absorbers," *J Acoust Soc Am*, vol. 24, no. 3, pp. 309–312, May 1952, doi: 10.1121/1.1906897.

[29] A. K. Kłosak, "Design, simulations and experimental research in the process of development of sound absorbing perforated ceiling tile," *Applied Acoustics*, vol. 161, Apr. 2020, doi: 10.1016/J.APACOUST.2019.107185.

[30] A. Gautam, A. Celik, and M. Azarpeyvand, "Double Degree of Freedom Helmholtz Resonator Based Acoustic Liners," in *AIAA AVIATION 2021 FORUM*, American Institute of Aeronautics and Astronautics , 2021. doi: https://doi.org/10.2514/6.2021-2205.

[31] R. Sugimoto, P. Murray, and R. J. Astley, "Folded cavity liners for turbofan engine intakes," in *18th AIAA/CEAS Aeroacoustics Conference (33rd AIAA Aeroacoustics Conference)*, American Institute of Aeronautics and Astronautics Inc., 2012. doi: 10.2514/6.2012-2291.

[32] M. XuQiang and S. ZhengTao, "Development of acoustic liner in aero engine: A review," vol. 63, pp. 2491–2504, 2020, doi: 10.1007/s11431-019-1501-3.

[33] Y. Tang *et al.*, "Hybrid acoustic metamaterial as super absorber for broadband low-frequency sound," *Sci Rep*, vol. 7, Feb. 2017, doi: 10.1038/srep43340.

[34] T. L. Parrott and M. G. Jones, "Cascaded Perforates as One-Dimensional, Bulk Absorbers," in *12th AIAA/CEAS Aeroacoustics Conference (27th AIAA Aeroacoustics Conference)*, Cambridge: American Institute of Aeronautics and Astronautics , 2006. doi: https://doi.org/10.2514/6.2006-2402.

[35] M. Dannemann *et al.*, "Experimental Study of Advanced Helmholtz Resonator Liners with Increased Acoustic Performance by Utilising Material Damping Effects", doi: 10.3390/app8101923.

[36] S. J. Estève and M. E. Johnson, "Adaptive Helmholtz resonators and passive vibration absorbers for cylinder interior noise control," *J Sound Vib*, vol. 288, no. 4–5, pp. 1105–1130, Dec. 2005, doi: 10.1016/J.JSV.2005.01.017.

[37] F. Liu, "A Tunable Electromechanical Helmholtz Resonator," University of Florida, 2007. Accessed: Apr. 23, 2023. [Online]. Available: http://ufdcimages.uflib.ufl.edu/UF/E0/01/98/15/00001/liu_f.pdf

[38] K. Williams, G. Chiu, and R. Bernhard, "Adaptive-passive absorbers using shape-memory alloys," *J Sound Vib*, vol. 249, no. 5, pp. 835–848, Jan. 2003, doi: 10.1006/JSVI.2000.3496.

[39] B. C. White, A. Garland, R. Alberdi, and B. L. Boyce, "Interpenetrating lattices with enhanced mechanical functionality," *Addit Manuf*, vol. 38, Feb. 2021, doi: 10.1016/J.ADDMA.2020.101741.

[40] Gen3D, "Types of lattices for additive manufacturing - the terms all engineers need to know - Gen3D." https://gen3d.com/news-and-articles/types-of-lattices-for-additive-manufacturing/ (accessed Feb. 02, 2023).

[41] C. Pan, Y. Han, and J. Lu, "Design and Optimization of Lattice Structures: A Review", doi: 10.3390/app10186374.

[42] O. Al-Ketan, R. K. Abu Al-Rub, U. Abu Dhabi, and A. Dhabi, "MSLattice: A free software for generating uniform and graded lattices based on triply periodic minimal surfaces," 2020, doi: 10.1002/mdp2.205.

[43] O. Al-Ketan, D. W. Lee, R. Rowshan, and R. K. Abu Al-Rub, "Functionally graded and multi-morphology sheet TPMS lattices: Design, manufacturing, and mechanical properties," *J Mech Behav Biomed Mater*, vol. 102, Feb. 2020, doi: 10.1016/j.jmbbm.2019.103520.

[44] W. Yang, J. An, C. K. Chua, and K. Zhou, "Acoustic absorptions of multifunctional polymeric cellular structures based on triply periodic minimal surfaces fabricated by stereolithography," *Virtual Phys Prototyp*, vol. 15, no. 2, pp. 242–249, Apr. 2020, doi: 10.1080/17452759.2020.1740747.

[45] S. Deshmukh, H. Ronge, and S. Ramamoorthy, "Design of periodic foam structures for acoustic applications: Concept, parametric study and experimental validation," *Mater Des*, vol. 175, Aug. 2019, doi: 10.1016/j.matdes.2019.107830.

[46] M. G. Jones, T. L. Parrott, D. L. Sutliff, and C. E. Hughes, "Assessment of Soft Vane and Metal Foam Engine Noise Reduction Concepts," in *15th AIAA/CEAS Aeroacoustics Conference (30th AIAA Aeroacoustics Conference)*, Miami: American Institute of Aeronautics and Astronautics , Nov. 2012. doi: https://doi.org/10.2514/6.2009-3142.

[47] A. R. F. Li, D. I. W. Levin, D. Matusik, and W. Zheng, "Acoustic Voxels: Computational Optimization of Modular Acoustic Filters," *ACM Trans. Graph*, vol. 35, 2016, doi: 10.1145/2897824.2925960.

[48] W. Johnston and B. Sharma, "Additive Manufacturing of Fibrous Sound Absorbers," *Addit Manuf*, vol. 41, May 2021, doi: https://doi.org/10.1016/j.addma.2021.101984.

[49] L. Suárez and & María Del Mar Espinosa, "Assessment on the use of additive manufacturing technologies for acoustic applications", doi: 10.1007/s00170-020-05853-2/Published.

[50] A. R. Bailey, "The transmission line loudspeaker enclosure," *Wireless World*, vol. 215, 1972.

[51] J. J. Lechuga Aranda, S. Bader, and B. Oelmann, "A space-coiling resonator for improved energy harvesting in fluid power systems," *Sens Actuators A Phys*, vol. 291, pp. 58–67, Jun. 2019, doi: 10.1016/j.sna.2019.01.022.

[52] W. Yang *et al.*, "3D printing of polymeric multi-layer micro-perforated panels for tunable wideband sound absorption," *Polymers (Basel)*, vol. 12, no. 2, Feb. 2020, doi: 10.3390/polym12020360.

[53] A. Mirzendehdel and K. Suresh, *A Hands-on Introduction to Topology Optimization*, 1st ed. 2017.

[54] "GE jet engine bracket challenge | Engineering & Design Challenges | GrabCAD." https://grabcad.com/challenges/ge-jet-engine-bracket-challenge (accessed Mar. 11, 2023).

[55] F. M. Azevedo, M. S. Moura, W. M. Vicente, R. Picelli, and R. Pavanello, "Topology optimization of reactive acoustic mufflers using a bi-directional evolutionary optimization method," *Structural and Multidisciplinary Optimization*, vol. 58, no. 5, pp. 2239–2252, Nov. 2018, doi: 10.1007/S00158-018-2012-5/TABLES/3.

[56] L. L. Chen, H. Lian, S. Natarajan, W. Zhao, X. Y. Chen, and S. P. A. Bordas, "Multi-frequency acoustic topology optimization of sound-absorption materials with isogeometric boundary element methods accelerated by frequency-decoupling and model order reduction techniques," *Comput Methods Appl Mech Eng*, vol. 395, May 2022, doi: 10.1016/J.CMA.2022.114997.

[57] C. B. Dilgen, S. B. Dilgen, N. Aage, and J. S. Jensen, "Topology optimization of acoustic mechanical interaction problems: a comparative review," *Structural and Multidisciplinary Optimization*, vol. 60, no. 2, pp. 779–801, Aug. 2019, doi: 10.1007/S00158-019-02236-4/FIGURES/22.

[58] W. Chen, D. Lee, and O. Balogun, "GAN-DUF: Hierarchical Deep Generative Models for Design Under Free-Form Geometric Uncertainty," 2022, doi: https://doi.org/10.48550/arXiv.2202.10558.

[59] J. Kook and J. S. Jensen, "Topology optimization of periodic microstructures for enhanced loss factor using acoustic–structure interaction," *Int J Solids Struct*, vol. 122–123, pp. 59–68, Sep. 2017, doi: 10.1016/J.IJSOLSTR.2017.06.001.

[60] A. A. Giunta, M. S. Eldred, L. P. Swiler, T. G. Trucano, and S. F. Wojtkiewicz, "Perspectives in Optimization Under Uncertainty: Algorithms and Applications," in *10th AIAA/ISSMO Multidisciplinary Analysis and Optimization Conference*, Albuquerque: American Institute of Aeronautics and Astronautics , Jun. 2012. doi: https://doi.org/10.2514/6.2004-4451.

[61] D. M. Nark and M. G. Jones, "An acoustic liner design methodology based on a statistical source model," *Int J Aeroacoust*, vol. 20, no. 5–7, pp. 441–457, Sep. 2021, doi: 10.1177/1475472X211023874.

[62] Gen3D, "The seven categories of additive manufacturing technologies - Gen3D," Mar. 07, 2022. https://gen3d.com/news-and-articles/the-seven-categories-of-am-processes/ (accessed Mar. 16, 2023).

[63] Hybrid Manufacturing Technologies, "7 Families of Additive Manufacturing." https://hybridmanutech.com/resources/ (accessed Mar. 07, 2023).

[64] J. Ding, M. Baumers, E. A. Clark, and R. D. Wildman, "The economics of additive manufacturing: Towards a general cost model including process failure," *Int J Prod Econ*, vol. 237, Jul. 2021, doi: 10.1016/J.IJPE.2021.108087.

[65] Altair Engineering, “Design for Additive Manufacturing | Altair Inspire Print3D.” https://www.altair.com/inspire-print3d/ (accessed Apr. 23, 2023).

[66] M. Gouge and P. Michaleris, *Thermo-Mechanical Modeling of Additive Manufacturing*. Elsevier, 2018. doi: https://doi.org/10.1016/C2016-0-00317-0.

[67] M. Bayat *et al.*, “Part-scale thermo-mechanical modelling of distortions in Laser Powder Bed Fusion – Analysis of the sequential flash heating method with experimental validation,” *Addit Manuf*, vol. 36, Dec. 2020, doi: 10.1016/J.ADDMA.2020.101508.

[68] S. Sadeghi Borujeni, A. Shad, K. Abburi Venkata, N. Günther, and V. Ploshikhin, “Numerical simulation of shrinkage and deformation during sintering in metal binder jetting with experimental validation,” *Mater Des*, vol. 216, Apr. 2022, doi: 10.1016/J.MATDES.2022.110490.

[69] Iowa State University Center for Nondestructive Evaluation, “Nondestructive Evaluation Techniques : Radiography.” https://www.nde-ed.org/NDETechniques/Radiography/AdvancedTechniques/computedtomography.xhtml (accessed Mar. 15, 2023).

[70] F. H. Kim, A. L. Pintar, S. P. Moylan, and E. J. Garboczi, “The Influence of X-Ray Computed Tomography Acquisition Parameters on Image Quality and Probability of Detection of Additive Manufacturing Defects”, doi: 10.1115/1.4044515.

[71] S. Joshi, “Reverse Engineering.” 2018. Accessed: Apr. 23, 2023. [Online]. Available: https://psu.instructure.com/courses/2136290/pages/reverse-engineering-%7C-lecture-related-powerpoint-presentation?module_item_id=32833273

[72] “Optical Profilometry | Materials Research Institute.” https://www.mri.psu.edu/materials-characterization-lab/characterization-techniques/optical-profilometry (accessed Mar. 18, 2023).

[73] M. G. Jones, W. R. Watson, D. M. Nark, B. M. Howerton, and M. C. Brown, “A Review of Acoustic Liner Experimental Characterization at NASA Langley,” Hampton, Apr. 2020. Accessed: Apr. 23, 2023. [Online]. Available: https://ntrs.nasa.gov/citations/20200003112

[74] F. B. Neal and J. C. Russ, *Measuring Shape*. Taylor & Francis, 2017. doi: 10.1201/b12092.

[75] M. A. Machado, M. I. Silva, A. P. Martins, M. S. Carvalho, and T. G. Santos, “Double active transient thermography,” *NDT & E International*, vol. 125, p. 102566, Jan. 2022, doi: 10.1016/J.NDTEINT.2021.102566.

[76] “Standard Test Method for Impedance and Absorption of Acoustical Materials Using a Tube, Two Microphones and a Digital Frequency Analysis System.” doi: 10.1520/E1050-19.

[77] “Acoustics Module User’s Guide,” 2017. Accessed: Apr. 23, 2023. [Online]. Available: https://doc.comsol.com/5.3/doc/com.comsol.help.aco/AcousticsModuleUsersGuide.pdf

[78] S. Khurana, "Equivalent Fluid Modelling of a Honeycomb Acoustic Liner using the Acoustic Porous Medium Formulation," Delft University of Technology, Delft, 2020. [Online]. Available: http://repository.tudelft.nl/.

[79] National Center for Health Statistics, "Anthropometric Reference Data for Children and Adults: United States, 2015–2018," Washington, DC, 2021. Accessed: Mar. 17, 2023. [Online]. Available: https://www.cdc.gov/nchs/products/index.htm.

[80] Gramacy, *Gaussian process modeling, design and optimization for the applied sciences*. CRC Press, 2023.

[81] A. Forrester, A. Sobester, and A. Keane, *Engineering Design via Surrogate Modelling*. John Wiley & Sons Ltd., 2008.

[82] P. Maurerlehner, "AcousticPDE - openCFS User Documentation." https://opencfs.gitlab.io/userdocu/PDEExplanations/Singlefield/AcousticPDE/ (accessed Feb. 02, 2023).

[83] A. Papst, "LinFlowPDE - openCFS User Documentation." https://opencfs.gitlab.io/userdocu/PDEExplanations/Singlefield/LinFlowPDE/ (accessed Mar. 16, 2023).

[84] P. Virtanen *et al.*, "SciPy 1.0: Fundamental Algorithms for Scientific Computing in Python," *Nat Methods*, vol. 17, pp. 261–272, 2020, doi: 10.1038/s41592-019-0686-2.

[85] B. M. Adams *et al.*, "Dakota, A Multilevel Parallel Object-Oriented Framework for Design Optimization, Parameter Estimation, Uncertainty Quantification, and Sensitivity Analysis: Version 6.16 User's Manual," Albuquerque, 2022.

[86] H. Hassanpour, "TESTSUIT/Singlefield/LinFlow/ViscousChannel-ABC · master · openCFS / Testsuite · GitLab." https://gitlab.com/openCFS/Testsuite/-/tree/master/TESTSUIT/Singlefield/LinFlow/ViscousChannel-ABC (accessed Mar. 18, 2023).

[87] J. Schindelin *et al.*, "Fiji: an open-source platform for biological-image analysis," *Nat Methods*, vol. 9, no. 7, pp. 676–682, Jul. 2012, doi: 10.1038/nmeth.2019.

[88] D. Montgomery, *Introduction to Statistical Quality Control*, 6th ed. Hoboken: Wiley, 2009.

[89] B. M. Howerton and M. G. Jones, "A conventional liner acoustic/drag interaction benchmark database," in *23rd AIAA/CEAS Aeroacoustics Conference, 2017*, American Institute of Aeronautics and Astronautics Inc, AIAA, 2017. doi: 10.2514/6.2017-4190.

[90] S. Schoder and K. Roppert, "openCFS: Open Source Finite Element Software For Coupled Field Simulation - Part Acoustics," Jul. 2022, doi: https://doi.org/10.48550/arXiv.2207.04443.

[91] L. Jaouen, "Motionless Skeleton Models - APMR." https://apmr.matelys.com/PropagationModels/MotionlessSkeleton/index.html (accessed Mar. 19, 2023).

[92] M. Kaltenbacher and S. Schoder, “Computational Aeroacoustics Based on a Helmholtz-Hodge Decomposition,” in *SAE Technical Papers*, SAE International, Jun. 2018. doi: 10.4271/2018-01-1493.

[93] C. McCreight, “What equations are used to create the TPMS types? – nTopology,” Apr. 08, 2022. https://support.ntopology.com/hc/en-us/articles/360053267814-What-equations-are-used-to-create-the-TPMS-types- (accessed Feb. 02, 2023).

[94] R. Schmidt, “Implicit Surface Modeling — gradientspace,” Feb. 26, 2018. http://www.gradientspace.com/tutorials/2018/2/20/implicit-surface-modeling (accessed Apr. 23, 2023).

Appendix A

A.1 TPMS Equation Reference

This appendix documents a mathematical reference with some fundamental equations needed to generate and manipulate TPMS structures.

TPMS Equations adapted from [42], [43], [93], [94]

Schwarz P

$$F(x,y,z) = \cos(x) + \cos(y) + \cos(z) - C \tag{A-1}$$

Schwarz D

$$F(x,y,z) = \cos(x)\cos(y)\cos(z) - \sin(x)\sin(y)\sin(z) - C \tag{A-2}$$

Diamond

$$\begin{aligned} F(x,y,z) = {} & \sin(x)\sin(y)\sin(z) + \sin(x)\cos(y)\cos(z) \\ & + \cos(x)\sin(y)\cos(z) + \cos(x)\cos(y)\sin(z) - C \end{aligned} \tag{A-3}$$

Gyroid

$$F(x,y,z) = \sin(x)\cos(y) + \sin(y)\cos(z) + \sin(z)\cos(x) - C \tag{A-4}$$

Neovius

$$F(x,y,z) = 3(\cos(x) + \cos(y) + \cos(z)) + 4\cos(x)\cos(y)\cos(z) - C \tag{A-5}$$

Lidinoid

$$\begin{aligned} F(x,y,z) = {} & \sin(2x)\cos(y)\sin(z) + \sin(2y)\cos(z)\sin(x) \\ & + \sin(2z)\cos(x)\sin(y) - \cos(2x)\cos(2y) \\ & - \cos(2y)\cos(2z) - \cos(2z)\cos(2x) + 0.3 - C \end{aligned} \tag{A-6}$$

Split P

$$\begin{aligned} F(x,y,z) = 1.1(& \sin(2x)\sin(z)\cos(y) + \sin(2y)\sin(x)\cos(z) \\ & + \sin(2z)\sin(y)\cos(x)) \\ & - 0.2(\cos(2x)\cos(2y) + \cos(2y)\cos(2z) + \cos(2z)\cos(2)) \\ & - 0.4(\cos(2x) + \cos(2y) + \cos(2z)) - C \end{aligned} \tag{A-7}$$

IWP

$$F(x,y,z) = 2(\cos(x)\cos(y) + \cos(y)\cos(z) + \cos(z)\cos(x)) - (\cos(2x) + \cos(2y) + \cos(2z)) - C \qquad (A\text{-}8)$$

FRD

$$F(x,y,z) = 4(\cos(x)\cos(y)\cos(z)) - (\cos(2x)\cos(2y) + \cos(2y)\cos(2z) + \cos(2z)\cos(2x)) - C \qquad (A\text{-}9)$$

PMY

$$F(x,y,z) = 2\cos(x)\cos(y)\cos(z) + \sin(2x)\sin(y) + \sin(x)\sin(2z) + \sin(2y)\sin(z) - C \qquad (A\text{-}10)$$

S

$$F(x,y,z) = \cos(2x)\sin(y)\cos(z) + \cos(2y)\sin(z)\cos(x) + \cos(2z)\sin(x)\cos(y) - C \qquad (A\text{-}11)$$

Arc length unit cell sizing:

$$X, Y, Z = 2\pi(x, y, z) \qquad (A\text{-}12)$$

Convert from cartesian coordinates to cylindrical coordinates:

$$r_c = \sqrt{x^2 + y^2} \qquad (A\text{-}13)$$

$$\vartheta_c = \tan^{-1}\left(\frac{y}{x}\right) \qquad (A\text{-}14)$$

$$z_c = z_c \qquad (A\text{-}15)$$

Convert from cartesian coordinates to spherical coordinates:

$$r_s = \sqrt{x^2 + y^2 + z^2} \qquad (A\text{-}16)$$

$$\vartheta_s = \tan^{-1}\left(\frac{y}{x}\right) \tag{A-17}$$

$$\varphi_s = \cos^{-1}\left(\frac{z}{\sqrt{x^2+y^2+z^2}}\right) \tag{A-18}$$

Hybrid multi-morphology TPMS blending with different unit cell types:

$$F_{Dual-TPMS} = GF_1 + (1-G)F_2 \tag{A-19}$$

$$F_{Multi-TPMS} = \sum_{u=1}^{n} \frac{1+e^{b\|x-x_u\|^2}}{\sum_{i=1}^{n} 1+e^{b\|x-x_i\|^2}} F_u \tag{A-20}$$

Boolean operations:

$$F_{combine} = \min(F_1, F_2) \tag{A-21}$$

$$F_{subtract} = \max(F_1, -F_2) \tag{A-22}$$

$$F_{intersection} = \max(F_1, F_2) \tag{A-23}$$

Appendix B

B.1 Liner Assembly Template Dimensions and Unit Cell Specifications

This appendix shows the dimensions and specifications of the eight different AM acoustic liner design concepts from Chapter 4.

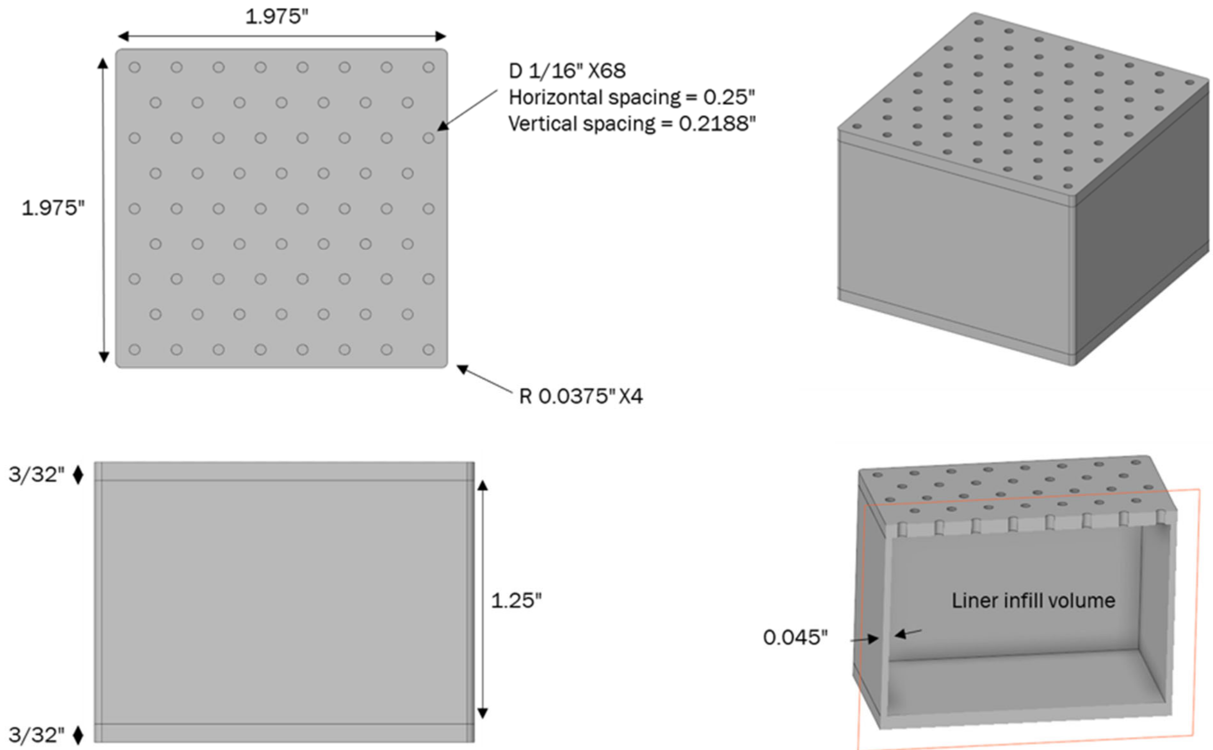

Figure B-1. Liner design template dimensions.

Table B-1. Chapter four unit cell design specifications.

Design	Unit Cells X	Unit Cells Y	Unit Cells Z	Volume Fraction	Thickness (in)
Schwarz P	4.5	4.5	4.5	0.3677	0.045
Schwarz D	3	3	3	0.1665	0.045
Gyroid	4	4	4	0.1851	0.045
Hex	6	6.5	1	0.2393	0.045
Conical Spiral	7.5	4.5	1	0.1139	0.045
Lidinoid	3	3	3	0.2730	0.045
Split P	3	3	3	0.1875	0.045
Voronoi Lattice	1	1	1	0.1437	0.045